J. Fluid Mech. (1995), *vol.* 296, *pp.* 271–324

A nonlocal theory for stress in bound, Brownian suspensions of slender, rigid fibres

By RICHARD L. SCHIEK AND ERIC S. G. SHAQFEH

Department of Chemical Engineering, Stanford University, Stanford, CA 94305–5025, USA

(Received 6 September 1994 and in revised form 3 February)

A nonlocal theory for stress in bound suspensions of rigid, slender fibres is developed and used to predict the rheology of dilute, rigid polymer suspensions when confined to capillaries or fine porous media. Because the theory is nonlocal, we describe transport in a fibre suspension where the velocity and concentration fields change rapidly on the fibre's characteristic length. Such rapid changes occur in a rigidly bound domain because suspended particles are sterically excluded from configurations near the boundaries. A rigorous no-flux condition resulting from the presence of solid boundaries around the suspension is included in our nonlocal stress theory and naturally gives rise to concentration gradients that scale on the length of the particle. Brownian motion of the rigid fibres is included within the nonlocal stress through a Fokker–Planck description of the fibres' probability density function where gradients of this function are proportional to Brownian forces and torques exerted on the suspended fibres. This governing Fokker–Planck probability density equation couples the fluid flow and the nonlocal stress resulting in a nonlinear set of integral-differential equations for fluid stress, fluid velocity and fibre probability density. Using the method of averaged equations (Hinch 1977) and slender-body theory (Batchelor 1970), the system of equations is solved for a dilute suspension of rigid fibres experiencing flow and strong Brownian motion while confined to a gap of the same order in size as the fibre's intrinsic length. The full solution of this problem, as the fluid in the gap undergoes either simple shear or pressure-driven flow, is solved self-consistently yielding average fluid velocity, shear and normal stress profiles within the gap as well as the probability density function for the fibres' position and orientation. From these results we calculate concentration profiles, effective viscosities and slip velocities and compare them to experimental data.

1. Introduction

In many important natural and industrial processes, suspensions are confined to flow within domains whose size is comparable to that of the suspended particle. In living organisms the circulation of blood carries cells and macromolecules through small capillaries while separation technologies like chromatography convey suspensions through fine porous media. While passing through a fine pore, a suspended particle responds to a radically different environment than if it were in a bulk suspension. Flowing through a small domain, the particle can experience concentration gradients and fluid velocity fields that change rapidly over its intrinsic length. Additionally, the Brownian force and torque felt by a particle can be different in magnitude if the particle is near a boundary or a distance on the order of the particle length away from the boundary.

The complexity of the flow is primarily a consequence of the confining geometry. When a suspended particle is flowing within a rigid domain whose size is comparable to that of the particle, positions and configurations are sterically excluded near the domain boundaries. Thus, there can be a depleted layer where the concentration of suspended particles drops from its bulk value to zero over a length comparable to the suspended particle's size. Experimental investigations (Müller-Mohnssen, Weiss & Tippe 1990) have verified the existence of this depleted layer and its effect on the bulk rheology of a suspension is well documented, (e.g. Chauveteau 1982; Cohen & Metzner 1985; Sorbie & Huang 1991; Vargas, Pérez-González & Romero-Barenque 1993). The primary finding of these experimental studies has been that the effective viscosity of the suspension decreases as the domain of the flow shrinks (Chauveteau 1982; Cohen & Metzner 1985; Sorbie & Huang 1991; Vargas *et al.* 1993). Conversely one can restate this general trend in terms of a slip velocity between the suspension and the rigid boundary. As the domain for flow decreases, the slip velocity tends to increase. Physically these trends are observed because the depleted layer near the boundary has a lower viscosity than the bulk suspension. This thin, low-viscosity layer allows the more viscous core of the suspension to slide over the bounding surface resulting in positive slip, or a lower effective viscosity.

Early theoretical work has attempted to model the depletion layer and its rheology by considering a Hookean dumbbell interacting with an external potential whose value is zero within the flow domain and infinite outside the domain. Considering simple shear between two infinite, parallel plates, Brunn (1976) calculated the probability density function for the end-to-end distance of a Hookean dumbbell assuming uniform simple shear and strong Brownian motion. With this probability density function, he calculated the extra stress created by the dumbbells and the expected first correction to the velocity profile. Brunn (1976) found that the velocity profile looked like simple shear in the centre of the channel in that it was linear and of constant shear rate. Within a dumbbell length of either wall the shear rate increased rapidly, making the velocity profile nonlinear in this region. This small region of high shear rate was interpreted as the slip region and a slip velocity was derived by extending the uniform velocity profile near the centre of the channel to the wall. As the channel width decreased, this slip velocity was found to increase, corresponding to a reduction of the effective viscosity as the separation between the plates decreased.

By considering the first effects of a Hookean dumbbell on a simple shear velocity profile between two infinite parallel plates, Brunn & Grisafi (1987) improved on the earlier theoretical work by finding analytical solutions for stress and velocity within very small and very large gaps. The same general trends were found as before in that the effective viscosity decreased as the channel width was reduced. Additionally, normal stresses were calculated and found to decrease from their bulk value monotonically to zero at the wall over a length comparable to the radius of gyration of the suspended dumbbell. Later, with the same model system, Aubert & Tirrell (1982) solved the problem self-consistently for the fluid velocity and effective viscosity, finding the same general trends.

Working with the model system of a Hookean dumbbell under simple shear between two infinite, parallel plates, Mavrantzas & Beris (1992) modelled the rheology of this system by constructing a Hamiltonian and then minimizing the Helmholtz free energy. Supporting the earlier findings (Aubert & Tirrell 1982; Brunn & Grisafi 1987) they found first normal stress differences that monotonically decreased from their bulk values in the centre of the gap to zero at the walls, and slip velocities in-

creased as the channel width decreased. Additionally, they found a monotonically decreasing dumbbell concentration over the distance of one dumbbell length near the walls. While their results confirm earlier findings (Aubert & Tirrell 1982; Brunn 1976; Brunn & Grisafi 1987), the methodology used is amenable to more complex geometries and implies that these broad trends apply there as well.

The model problem considered in this work is a suspension of slender rigid fibres experiencing either shear or pressure-driven flow and strong Brownian motion while they are confined between two infinite, parallel plates. In §2 using slender body theory (Batchelor 1970), averaged equations (Hinch 1977) and nonlocal transport theory (Shaqfeh 1988), the ensemble-average extra stress due to the fibres is constructed in terms of an integral average of the velocity gradient and the probability density function describing the fibre positions and orientations. This extra stress formulation inherently allows for velocity fields and concentration gradients that change on the length of a fibre. In addition we allow for a general torque (such as a Brownian torque) to be exerted on the fibre. Thus, this extra stress captures the physics of the environment felt by a fibre in or near a depletion layer where the velocity and concentration are changing rapidly. When the environment around the fibre is constant in concentration and velocity gradient, the nonlocal extra stress reduces to a classical, volume-averaged extra stress and we recover the theoretical results for unbound, homogeneous suspensions of rigid fibres (Brenner 1974; Giesekus 1962; Hinch & Leal 1972).

To complete the description of the extra stress, the governing Fokker-Plank equation for the probability density function describing the fibre positions and orientations is derived in §3. Since the probability density function depends on the fibre's centre-of-mass translational and its rotational velocity which both depend on integrals of the fluid velocity, this governing equation is coupled to the fluid motion. Because this governing probability density equation describes an unbound fluid domain additional boundary conditions are required for the bound model system considered here. Using rigorous no-flux boundary conditions developed elsewhere (Nitsche & Brenner 1990; Nitsche 1991), the probability density function is completely specified. This is accomplished without the addition of an external potential to model the steric hindrance of the walls.

The governing momentum equations for the suspension are derived in §4 and incorporated into the model because both the nonlocal, average extra stress and probability density function depend on the average fluid velocity field. This leaves the solution of a coupled set of nonlinear, integral-differential equations to find the average velocity, stress and the fibre's probability density function. In §5 the methods used to solve this system of equations are discussed. First the model problem is solved for simple shear flow and these results are presented in §6. Additionally, simple theories which are asymptotically correct for zero concentration and small gap width are developed in §6 and compared to the full, nonlocal theory. Results for pressure-driven flow are given in §7 along with small concentration and small gap asymptotic theories. Detailed comparisons are made between our theoretical predictions and previous experimental results in §8. Finally, concluding remarks and questions for further study are discussed in §9.

2. Derivation of the nonlocal stress

To describe the rigid fibres considered in this work, the notation shown in figure 1(*a*) will be used. Each fibre has a length of 2ℓ and a diameter of $2b$. The fibre's aspect

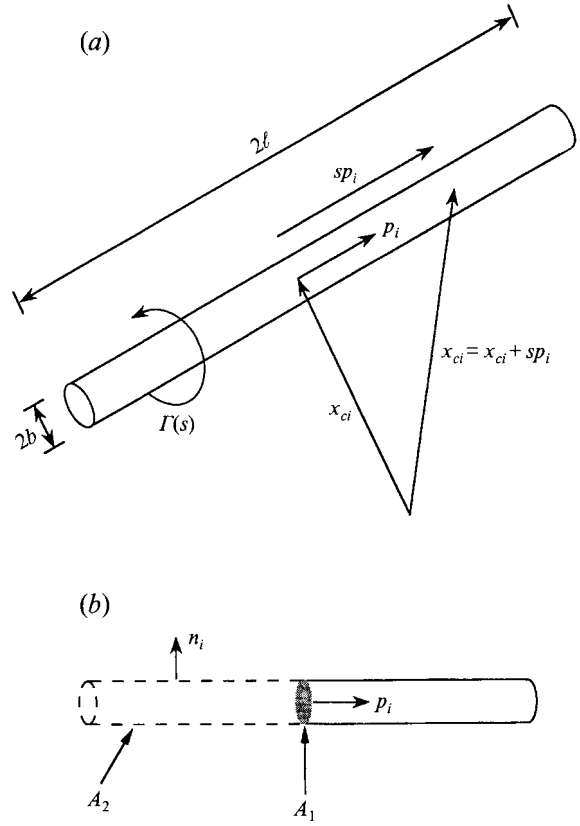

FIGURE 1. (*a*) Notation used to describe a fibre. (*b*) Force balance on a fibre.

ratio (ℓ/b) is assumed to be large such that its inverse is small, $\varepsilon \equiv b/\ell \ll 1$. A fibre's centre-of-mass location is denoted in index notation by the Cartesian vector x_{ci}. Similarly, a fibre's orientation is given by the Cartesian unit vector p_i which is parallel to the fibre's major axis. When x_i is defined as $x_i = x_{ci} + s\,p_i$ as shown graphically in figure 1(*a*), the scalar s locates points along the fibre's central axis for all s in the range $-\ell$ to $+\ell$. At any axial position s, the function $\Gamma(s)$ denotes the fibre's cross-sectional perimeter. For a fibre with centre-of-mass position $\boldsymbol{x}_c$ and orientation $\boldsymbol{p}$, $D(\boldsymbol{x}_c, \boldsymbol{p})$ is the set of all points that lie within the fibre. Finally, the number density of fibres in the suspension is n.

Considering a suspension of rigid fibres in a Newtonian solvent, the total stress at a point within a given realization of the suspension can be determined from the definition of stress for a Newtonian solution plus the extra stress caused by the presence of the fibres as

$$\sigma_{ij} = -\mathscr{P}\,\delta_{ij} + 2\mu\,e_{ij} + \sigma'_{ij} \tag{2.1}$$

where $\mathscr{P}$ is the fluid pressure, δ_{ij} is the isotropic unit tensor, μ is the Newtonian solvent viscosity, e_{ij} is the rate of strain tensor and σ'_{ij} is the extra stress due to the presence of the fibres in the suspension. Because rigid fibres do not, in general, obey a Newtonian stress relation, σ'_{ij} is defined as a generalized function which is zero whenever the point of interest lies outside a fibre and is finite within a fibre. With

this definition of the extra stress, the expression for the total stress is exact for any single configuration of fibres in the suspension.

Within a fibre suspension, a specific fibre configuration has a frequency, or probability of occurrence. Given a complete fibre suspension configuration, an instantaneous extra stress and bulk stress can be calculated. To obtain an average behaviour for the system, one of two approaches can be followed. Average behaviour can be determined by following one configuration of fibres over a long period of time and averaging over this sampling time; such would be an ergodic approach. Another approach is to consider all possible configurations of fibres in the suspension along with each configurations' probability of occurring. The average stress, or extra stress in this framework is the sum of all the products of the instantaneous stress due to a configuration and the probability of occurrence of that specific configuration. This latter method is know as ensemble averaging.

To obtain more general results, equation (2.1) is averaged over all allowed configurations, or ensembles, of fibres within the suspension. Ensemble averaging equation (2.1) as defined by McQuarrie (1976) and using $\langle\cdot\rangle$ brackets to denote ensemble averaged quantities yields

$$\langle\sigma_{ij}\rangle = -\langle\mathscr{P}\rangle\,\delta_{ij} + 2\mu\,\langle e_{ij}\rangle + \langle\sigma'_{ij}\rangle\,. \tag{2.2}$$

For the Newtonian components of the stress, the ensemble averages are easily completed because the medium is unaffected by the configuration of the fibres. However, the extra stress term depends strongly on fibre configuration. Applying the definition of an ensemble average and noting that the extra stress is zero outside a fibre, the ensemble averaged extra stress is

$$\langle\sigma'_{ij}\rangle(\boldsymbol{x}) = \int_{\Omega} \mathrm{d}\boldsymbol{p} \int_{\boldsymbol{x}\in D(\boldsymbol{x}_c,\boldsymbol{p})} \mathrm{d}\boldsymbol{x}_c\,\langle\sigma'_{ij}(\boldsymbol{x}|\boldsymbol{x}_c,\boldsymbol{p})\rangle_1\,P(\boldsymbol{x}_c,\boldsymbol{p})\,. \tag{2.3}$$

A similar expression was derived by Shaqfeh (1988) for the nonlocal, extra heat flux in a composite of highly conducting slender fibres. The similarity to Shaqfeh's work results from considering the fibres in nonlocal environments where the driving forces behind transport change on the same length scale as the size of a suspended particle, and in the use of conditionally averaged quantities as defined by Hinch (1977).

Since the average extra stress in equation (2.3), $\langle\sigma'_{ij}\rangle(\boldsymbol{x})$, can only depend on ensembles containing fibres that intersect the point of interest, $\boldsymbol{x}$, the domains of integration select a subset of configurations from all possible configurations of fibres in the suspension. Each member of this subset of ensembles contains a fibre that intersects the point of interest. For the first integral, the integration domain Ω is the set of all allowed orientations $\boldsymbol{p}$. The second integral's domain, $\boldsymbol{x}\in D(\boldsymbol{x}_c,\boldsymbol{p})$, is the set of centre-of-mass locations, $\boldsymbol{x}_c$, such that the point of interest, $\boldsymbol{x}$, lies within the domain of a fibre whose centre of mass is at $\boldsymbol{x}_c$ and has an orientation $\boldsymbol{p}$.

While the domains of integration in the formal definition of the extra stress select all ensembles that affect the point of interest $\boldsymbol{x}$, the integrals in equation (2.3) simply average the extra stress for a given fibre configuration. The averaging arises because the kernel weighs the stress for a given configuration, $\langle\sigma'_{ij}(\boldsymbol{x}|\boldsymbol{x}_c,\boldsymbol{p})\rangle_1$, with the probability for having that configuration, $P(\boldsymbol{x}_c,\boldsymbol{p})$, where terms enclosed by $\langle\cdot\rangle_1$ are first conditionally averaged quantities as defined by Hinch (1977). Physically $\langle\sigma'_{ij}(\boldsymbol{x}|\boldsymbol{x}_c,\boldsymbol{p})\rangle_1$, represents the extra stress at the point $\boldsymbol{x}$ given that there is a fibre with centre-of-mass position $\boldsymbol{x}_c$ and orientation $\boldsymbol{p}$, averaged over all possible positions and orientations of other fibres in the suspension. The final factor in equation (2.3), $P(\boldsymbol{x}_c,\boldsymbol{p})$, is a probability density function for fibre configuration in the suspension. The

normalization condition for this probability density function is fixed by conserving the fibre mass within the suspension. The integral of probability density over the complete fibre configuration space (all allowed $\boldsymbol{x}_c$ and $\boldsymbol{p}$) equals the number of fibres in the suspension since all the suspended fibres lie within the configuration space. Specifically, the normalization condition is

$$\int_V \mathrm{d}\boldsymbol{x}_c \int_\Omega \mathrm{d}\boldsymbol{p} P(\boldsymbol{x}_c, \boldsymbol{p}) = N, \tag{2.4}$$

where N is the total number of fibres in the domain V of the suspension, and it can be seen that the probability density function has the dimensions of number per unit volume.

Within a slender rigid fibre, gradients of the extra stress are much larger along the fibre's length than perpendicular to it. For a fibre aligned parallel to the x_1 axis, this implies

$$\frac{\partial \langle \sigma'_{ij} \rangle}{\partial x_1} \gg \frac{\partial \langle \sigma'_{ij} \rangle}{\partial x_2}, \frac{\partial \langle \sigma'_{ij} \rangle}{\partial x_3}. \tag{2.5}$$

The kernel of equation (2.3) will not change appreciably as the centre-of-mass position $\boldsymbol{x}_c$ is displaced by a fibre radius b perpendicular to the fibre's central axis provided the probability density function is constant over these same centre-of-mass displacements. As the aspect ratio increases (making $b/\ell \ll 1$), an $O(b)$ translation of $\boldsymbol{x}_c$ perpendicular to $\boldsymbol{p}$ negligibly changes the centre-of-mass. Thus $\boldsymbol{x}_c \approx \boldsymbol{x} - s\boldsymbol{p}$ where $s \in [-\ell, +\ell]$ defines all centre of mass positions for a given orientation of fibres that intersect the point of interest to within an $O(b)$ distance. Integrating equation (2.3) over all centre-of-mass displacements of $O(b)$ perpendicular to $\boldsymbol{p}$ is equivalent to integrating over a fibre cross-section and results in

$$\langle \sigma'_{ij} \rangle (\boldsymbol{x}) = \int_\Omega \mathrm{d}\boldsymbol{p} \int_{-\ell}^{+\ell} \mathrm{d}s \langle \bar{\sigma}'_{ij} (\boldsymbol{x} | \boldsymbol{x} - s\boldsymbol{p}, \boldsymbol{p}) \rangle_1 P(\boldsymbol{x} - s\boldsymbol{p}, \boldsymbol{p}), \tag{2.6}$$

where $\langle \bar{\sigma}'_{ij} \rangle_1$ is the conditionally averaged extra stress integrated over a cross-section of a fibre and has dimensions of force per unit length.

To determine $\langle \bar{\sigma}'_{ij} \rangle$, we seek a connection between this conditionally averaged quantity and a physical force per unit length experienced by a fibre. Considering a force balance on a section of a force-free rod as shown in figure 1(b) and neglecting the ends of the rod, one finds

$$\int \sigma^R_{ij} p_j \, \mathrm{d}A_1 + \int \sigma^F_{ij} n_j \, \mathrm{d}A_2 = 0, \tag{2.7}$$

where σ^R_{ij} is the stress inside the rod, p_j is the rod's orientation vector which is perpendicular to the cross-section of the rod, σ^F_{ij} is the fluid stress at the rod's surface and n_j is the local normal outward to the rod's surface. Equation (2.7) states that the force transmitted through the cross-section of a rod (area A_1) must be balanced by the force exerted on the surface of the rod (area A_2), cf. figure 1(b). The orientation of the fibre, p_j, does not depend on the surface domain A_1 so the first integral can be completed as

$$\int \sigma^R_{ij} p_j \, \mathrm{d}A_1 = \bar{\sigma}'_{ij} p_j, \tag{2.8}$$

where $\bar{\sigma}'_{ij}$ is the extra stress integrated over a cross-section but not yet conditionally averaged. For a given position along the fibre's primary axis, the second integral in

equation (2.7) can be written as an integral of the fluid stress around the perimeter of the fibre integrated up to the location of the cross-section. Thus, the second integral in equation (2.7) becomes

$$\int \sigma_{ij}^F n_j \, \mathrm{d}A_2 = \int_{-\ell}^{s} \mathrm{d}\hat{s} \oint_{\Gamma(\hat{s})} \sigma_{ij}^F \left(\hat{s}|\boldsymbol{x}_c, \boldsymbol{p}\right) n_j \, \mathrm{d}\Gamma \tag{2.9}$$

$$= \int_{-\ell}^{s} \mathrm{d}\hat{s} \, f_i \left(\hat{s}|\boldsymbol{x}_c, \boldsymbol{p}\right), \tag{2.10}$$

where in moving from equation (2.9) to (2.10) one simply notices that the line integral about the perimeter in equation (2.9) is equivalent to the force per unit length, f_i, exerted by the fluid on the fibre.

Combining equations (2.7), (2.8) and (2.10) we can relate the extra stress integrated over a fibre cross-section to the force per unit length exerted by the fluid on a fibre:

$$\overline{\sigma}'_{ij} \left(s|\boldsymbol{x}_c, \boldsymbol{p}\right) = -\int_{-\ell}^{s} \mathrm{d}\hat{s} \, f_i \left(\hat{s}|\boldsymbol{x}_c, \boldsymbol{p}\right) p_j. \tag{2.11}$$

The deviatoric extra stress can be calculated by subtracting a third of the trace as $\frac{1}{3}\delta_{ij}\overline{\sigma}'_{kk}$. The derivation will be conducted with the non-deviatoric stress since the conversion to the deviatoric stress can be done at any point in the analysis and would necessitate carrying around extra, complicating terms.

This basic form for the extra stress was encountered earlier (Kirkwood & Riseman 1948; Riseman & Kirkwood 1950). In attempting to predict intrinsic viscosities for suspensions of flexible and rigid polymers, they derived an extra shear stress proportional to integrals of the force density on a polymer chain. Equation (2.11) is equivalent to that found in their formalism when evaluated over an entire rod length ($s = +\ell$). Specifically, the quantity $\overline{\sigma}'_{ij} \left(+\ell|\boldsymbol{x}_c, \boldsymbol{p}\right)$ is identical in structure to Kirkwood & Riseman's assertion that the primary source of extra stress is the force transmitted parallel to the fibre axis. On physical grounds, it can be argued that force transmitted along a rigid fibre's primary axis will always be $O(\ell/b)$ greater than force transmitted perpendicular to the primary axis since the force conduction length along the main axis is always $O(\ell/b)$ greater than lengths perpendicular to the main axis. For the large aspect ratio particles considered here, forces transmitted parallel to the fibre axis will be the dominant contributors to the extra stress.

Additional support for using an extra stress proportional to $-f_i \, p_j$ as in equation (2.11) can be found in the work of Shaqfeh & Fredrickson (1990). In that work the authors described transport in unbound suspensions of rigid rods by deriving an ensemble-averaged Green's function for the transport of momentum via a diagrammatic representation of multiple scattering events within the suspension. The Fourier space Green's function derived in their work implicitly contains information on the structure and scaling of the extra stress. Using the form of the extra stress in equation (2.11) and transforming to the governing equations of Shaqfeh & Fredrickson, one can derive a Green's function of the same structure as Shaqfeh & Fredrickson's. If the full extra stress derived at the end of this section is Fourier transformed, and substituted into their governing equations, their Green's function is exactly recovered. It is important to note that two completely different lines of reasoning arrive at the same results for unbound suspensions. While Shaqfeh & Fredrickson employed multiple scattering expansions to derive an ensemble-average Green's function, we recover their results using nonlocal theory and the method of averaged equations for an unbound non-Brownian suspension of rigid fibres.

The extra stress at a fibre's cross-sectional position s is related to a general force per unit length experienced by the fibre as shown in equation (2.11). More importantly, this expression for the extra stress at a cross-section depends parametrically on the fibre's centre-of-mass position $\boldsymbol{x}_c$ and orientation $\boldsymbol{p}$. For a dilute suspension where isolated particles do not interact, the leading-order solution for a first conditionally averaged field is equivalent to the disturbance field generated by a single particle (Hinch 1977; Shaqfeh 1988). Thus, in the dilute limit where $n\ell^3 \ll 1$, $\overline{\sigma}'_{ij}$ in equation (2.11) is equivalent to the first conditionally averaged extra stress integrated over a cross-section, cf. equation (2.6). Combining equations (2.6) and (2.11), one obtains the ensemble-average extra stress for a dilute suspension of fibres in terms of the force per unit length exerted by the fluid on a fibre in a given configuration weighted by the probability of having a fibre in that configuration:

$$\langle \sigma'_{ij} \rangle (\boldsymbol{x}) = -\int_{\Omega} \mathrm{d}\boldsymbol{p} \int_{-\ell}^{+\ell} \mathrm{d}s \int_{-\ell}^{s} \mathrm{d}\hat{s}\, P(\boldsymbol{x} - s\boldsymbol{p}, \boldsymbol{p})\, f_i\left(\hat{s}|\boldsymbol{x}_c, \boldsymbol{p}\right) p_j. \tag{2.12}$$

To relate the force per unit length in equation (2.12) to hydrodynamic forces and general body torques we use slender-body theory (Batchelor 1970; Shaqfeh & Fredrickson 1990). The primary result of this theory states that, when evaluated at the fibre surface, the disturbance velocity, u'_i, can be represented by an integral equation for the Stokeslet force density, $f_i(s)$, along the fibre's major axis as (Batchelor 1970),

$$\begin{aligned} u'_i &= u_i^{\infty} - U_i - s\dot{p}_i \\ &= \frac{1}{4\pi\mu}\left[\ln\left(2/\varepsilon\right) + \ln\left(\frac{\left[1-\left(s/\ell\right)^2\right]^{1/2}}{r(s)}\right)\right]\left(\delta_{ij}+p_ip_j\right)f_j \\ &\quad + \frac{1}{8\pi\mu}\left(\delta_{ij}-p_ip_j\right)f_j - \frac{1}{4\pi\mu}p_ip_jf_j \\ &\quad + \frac{1}{8\pi\mu}\left(\delta_{ij}+p_ip_j\right)\int_{-\ell}^{+\ell}\frac{f_j(s')-f_j(s)}{|s'-s|}\mathrm{d}s', \end{aligned} \tag{2.13}$$

where $r(s)$ is a dimensionless cross-sectional shape function defined by Batchelor (1970), while U_i and $\dot{p}_i$ are respectively the translational and rotational velocities of the fibre. We first consider fibres which are force free but may be under an applied torque denoted by $\mathcal{N}_i$. Thus, the Stokeslet force density is constrained by the following force and torque conditions respectively:

$$\int_{-\ell}^{+\ell} f_i(s)\,\mathrm{d}s = 0, \tag{2.14}$$

$$\epsilon_{ijk}p_k\int_{-\ell}^{+\ell} sf_j(s)\,\mathrm{d}s = \mathcal{N}_i, \tag{2.15}$$

where ϵ_{ijk} is the alternating unit tensor. By expanding f_i, U_i and $\dot{p}_i$ in the small parameter $\ln\left(2/\varepsilon\right)^{-1}$ as

$$\begin{aligned} f_i &= \ln\left(2/\varepsilon\right)^{-1} f_i^{(0)} + \ln\left(2/\varepsilon\right)^{-2} f_i^{(1)} + \cdots, \\ U_i &= U_i^{(0)} + \ln\left(2/\varepsilon\right)^{-1} U_i^{(1)} + \cdots, \\ \dot{p}_i &= \dot{p}_i^{(0)} + \ln\left(2/\varepsilon\right)^{-1} \dot{p}_i^{(1)} + \cdots, \end{aligned}$$

and substituting into equations (2.13), (2.14) and (2.15), the following leading-order

solutions for force density, $f_i^{(0)}$, centre-of-mass translational velocity, $U_i^{(0)}$, and centre-of-mass rotational velocity, $\dot{p}_i^{(0)}$ are found:

$$f_i^{(0)}(s|\boldsymbol{x}_c,\boldsymbol{p}) = \frac{4\pi\mu}{\ln(2/\varepsilon)}(\delta_{ij}-p_ip_j)\left[u_j^{\infty}(\boldsymbol{x}_c+s\boldsymbol{p}) - U_j^{(0)}(\boldsymbol{x}_c,\boldsymbol{p}) - s\,\dot{p}_j^{(0)}(\boldsymbol{x}_c,\boldsymbol{p})\right], \tag{2.16}$$

$$U_j^{(0)}(\boldsymbol{x}_c,\boldsymbol{p}) = \frac{1}{2\ell}\int_{-\ell}^{+\ell} u_j^{\infty}(\boldsymbol{x}_c+\acute{s}\boldsymbol{p})\,\mathrm{d}\acute{s}, \tag{2.17}$$

$$\dot{p}_j^{(0)}(\boldsymbol{x}_c,\boldsymbol{p}) = (\delta_{jk}-p_jp_k)\left(\frac{3}{2\ell^3}\right)\int_{-\ell}^{+\ell}\acute{s}\,u_j^{\infty}(\boldsymbol{x}_c+\acute{s}\boldsymbol{p})\,\mathrm{d}\acute{s} - \left(\frac{3}{2\ell^3}\right)\left(\frac{\ln(2/\varepsilon)}{4\pi\mu}\right)\epsilon_{jkm}\,p_k\,\mathscr{N}_m(\boldsymbol{x}_c). \tag{2.18}$$

Substituting equations (2.16), (2.17) and (2.18) into equation (2.12), changing the order of integration several times and carrying out a number of algebraic simplifications, one can derive the following expression for the ensemble-averaged extra stress:

$$\begin{aligned}\langle\sigma'_{ij}\rangle = {} & \frac{2\pi\mu}{\ln(2/\varepsilon)}\int_{\Omega}\mathrm{d}\boldsymbol{p}\int_{-2\ell}^{+2\ell}\mathrm{d}\xi\;W_1(\xi)\;p_i\,p_j\,p_k\,p_l\,\frac{\partial\langle u_k\rangle}{\partial x_l}(\boldsymbol{x}+\xi\boldsymbol{p}) \\ & +\frac{2\pi\mu}{\ln(2/\varepsilon)}\int_{\Omega}\mathrm{d}\boldsymbol{p}\int_{-2\ell}^{+2\ell}\mathrm{d}\xi\;W_2(\xi)(\delta_{ik}-p_ip_k)\;p_j\,p_l\,\frac{\partial\langle u_k\rangle}{\partial x_l}(\boldsymbol{x}+\xi\boldsymbol{p}) \\ & -\frac{3}{2\ell^3}\int_{\Omega}\mathrm{d}\boldsymbol{p}\int_{-\ell}^{+\ell}\mathrm{d}s\left(\frac{s^2-\ell^2}{2}\right)P(\boldsymbol{x}-s\boldsymbol{p},\boldsymbol{p})\,\epsilon_{imn}\,p_j\,p_m\,\mathscr{N}_n(\boldsymbol{x}-s\boldsymbol{p}|\boldsymbol{p}).\end{aligned} \tag{2.19}$$

In equation (2.19), $W_1(\xi)$ and $W_2(\xi)$ are weighting functions defined as

$$W_1(\xi) = \begin{cases}\displaystyle\int_{-\ell}^{\ell-\xi}\frac{(\ell-s)(\ell-\xi-s)}{2\ell}P(\boldsymbol{x}-s\boldsymbol{p},\boldsymbol{p})\,\mathrm{d}s & \text{for } \xi\geqslant 0\\ \displaystyle\int_{-\ell-\xi}^{\ell}\frac{(\ell-s)(\ell+\xi+s)}{2\ell}P(\boldsymbol{x}-s\boldsymbol{p},\boldsymbol{p})\,\mathrm{d}s & \text{for } \xi\leqslant 0\end{cases} \tag{2.20}$$

and

$$W_2(\xi) = \begin{cases}\displaystyle\int_{-\ell}^{\ell-\xi}\frac{(\ell+s)(-\ell+\xi+s)\left(-\ell^2-3s^2+3\ell\xi-3s\xi\right)}{4\ell^3}P(\boldsymbol{x}-s\boldsymbol{p},\boldsymbol{p})\,\mathrm{d}s & \text{for } \xi\geqslant 0,\\ \displaystyle\int_{-\ell-\xi}^{\ell}\frac{(\ell-s)(\ell+\xi+s)\left(\ell^2+3s^2+3\ell\xi+3s\xi\right)}{4\ell^3}P(\boldsymbol{x}-s\boldsymbol{p},\boldsymbol{p})\,\mathrm{d}s & \text{for } \xi\leqslant 0.\end{cases} \tag{2.21}$$

In the expression for the nonlocal extra stress, equation (2.19), the first two integral terms relate hydrodynamic forces to the total extra stress while the third term represents the contribution of a general body torque, $\mathscr{N}_n$, to the extra stress. The first integral term arises because a rigid fibre cannot stretch like a fluid line element. As the velocity gradient increases along the length of the fibre, the kernel $p_i\,p_j\,p_k\,p_l\,\partial u_k/\partial x_l$ grows, increasing its contribution to the extra stress. When the velocity gradients

and probability density function scale on lengths larger than the particle size, this first integral simplifies to become the classical bulk stress for an unbound, dilute suspension of slender, non-Brownian fibres derived by Batchelor (1971), and shown later in equation (2.27).

The second integral term in equation (2.19) arises from nonlocal rotational motions of fibres in the suspension. When the velocity field changes on lengths comparable to or smaller than a fibre's intrinsic length, the fibre cannot rotate with the fluid. Because of its rigidity, the fibre will rotate with an average value of the fluid velocity component perpendicular to its central axis. The kernel $(\delta_{ik} - p_i p_k) p_j p_l \partial u_k/\partial x_l$ selects gradients of the velocity field which are perpendicular to the fibre axis. When the velocity gradients and probability density function scale on lengths larger than the particle size, this term's contribution to the extra stress diminishes becoming zero as the velocity gradient and probability density of fibre configuration become uniform.

Both of the hydrodynamic terms in the extra stress definition, equation (2.19), contain weighting functions in their kernels defined by equations (2.20) and (2.21). The argument of the weighing functions, ξ, is a scalar distance in the direction of $\boldsymbol{p}$ from the point of interest $\boldsymbol{x}$ where the fluid velocity gradient is sampled, i.e. $\partial u_k/\partial x_l$ evaluated at $\boldsymbol{x}+\xi\boldsymbol{p}$. Thus as ξ varies from -2ℓ to $+2\ell$, the weighting functions control the degree to which the velocity gradient at $\boldsymbol{x} + \xi\boldsymbol{p}$ contributes to the extra stress.

Since both weighting functions $W_1(\xi)$ and $W_2(\xi)$ depend parametrically on the vectors $\boldsymbol{x}$ and $\boldsymbol{p}$ through the probability density function $P(\boldsymbol{x} - s\boldsymbol{p}, \boldsymbol{p})$, their shape and its importance are difficult to visualize. To better understand the weighting functions, we will temporarily assume that the suspension of fibres considered here is spatially homogeneous. If the suspension is spatially homogeneous, that is the fibres' centre-of-mass positions are random, then the probability density function, $P(\boldsymbol{x}_c, \boldsymbol{p})$, is independent of position and reduces to an orientation distribution function, $\Phi(\boldsymbol{p})$. Replacing $P(\boldsymbol{x}_c, \boldsymbol{p})$ with $\Phi(\boldsymbol{p})$ in equations (2.20) and (2.21) and factoring $\Phi(\boldsymbol{p})$ out of the weight function definition and into the extra stress expression, equation (2.19), one can analytically complete the integrals for the weighting functions. Under the condition of spatial homogeneity, the weighting functions become

$$W_1(\xi) = \frac{(2\ell - |\xi|)^3}{12\ell} \tag{2.22}$$

and

$$W_2(\xi) = \frac{(2\ell - |\xi|)^3 (8\ell^2 - 18\ell|\xi| - 3|\xi|^2)}{120\ell^3}. \tag{2.23}$$

Plotted in figures 2(*a*) and 2(*b*) as solid lines are the weighting functions of equations (2.22) and (2.23) respectively with fibre length, ℓ, set to unity. Examination of the graphs shows that both weighting functions $W_1(\xi)$ and $W_2(\xi)$ give strongest weight to the point of interest where $\xi = 0$. Moving away from the point of interest, $W_1(\xi)$ monotonically decreases, reaching zero identically at $\xi = \pm 2$. The weighting function $W_2(\xi)$ decreases rapidly away from $\xi = 0$, becoming negative before it identically reaches zero at $\xi = \pm 2$. Using the probability density function for a fibre in shear flow near a wall (calculated later in this paper) the form of the weighting functions can be examined for a particular position and orientation with a spatially dependent probability density function. Plotted in figures 2(*a*) and 2(*b*) as dashed lines are the weighting functions for a suspension with an inhomogeneous probability density function. While similar in structure to the

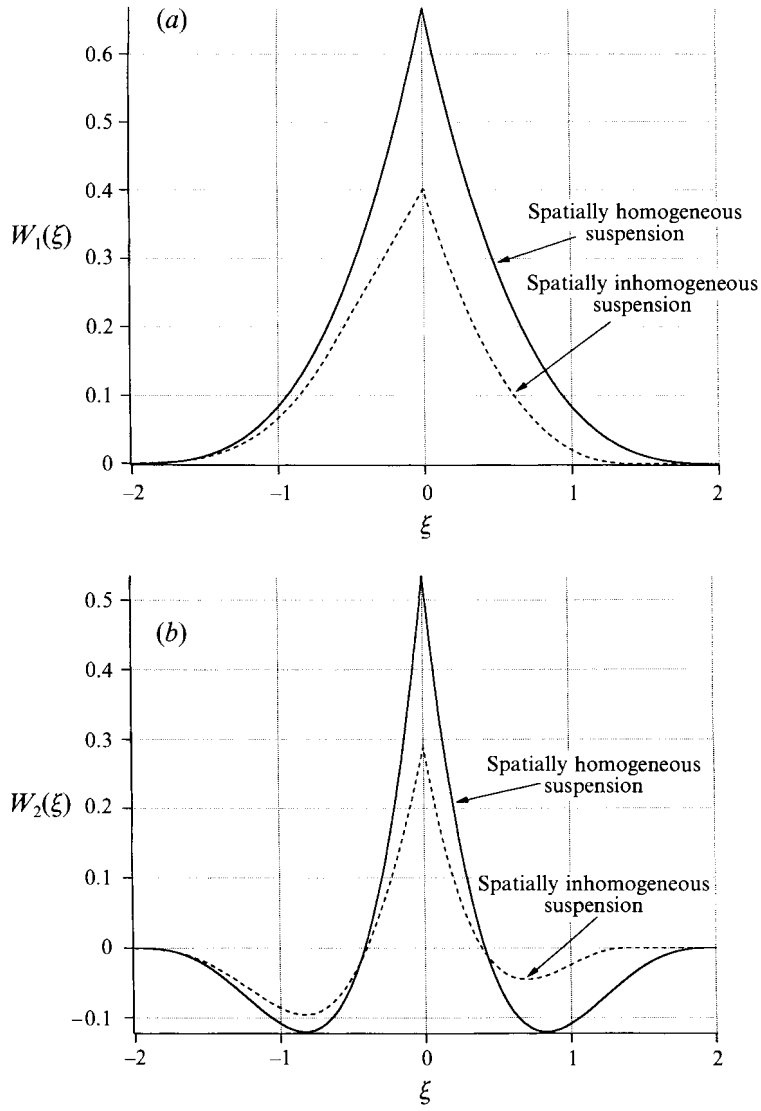

FIGURE 2. Weighting functions $W_1(\xi)$, in (*a*), and $W_2(\xi)$, in (*b*), plotted as a function of dimensionless distance along a fibre's major axis, ξ, where lengths have been made dimensionless with the fibre half-length ℓ.

spatially homogeneous weighting functions, the weighting functions for a spatially inhomogeneous suspension lack symmetry. Although still strongest at the point of interest, the nonlocal weighting functions are not necessarily symmetric about that point.

The third and final term in the extra stress expression, equation (2.19), relates a torque $\mathcal{N}_n$ on the suspended fibres to the extra stress. Inclusion of an external torque in the extra stress parallels inclusion of external torques in the governing equations for ferrofluids, suspensions in which an external magnetic field applies a torque to suspended particles (Rubí, Pérez-Madrid & Salueña 1990; Salueña, Pérez-Madrid & Rubí 1990). As with the hydrodynamic forces, the body torque included in the extra stress of equation (2.19) can vary on the length of the

suspended particle because it is treated nonlocally. To include Brownian torques within this extra stress, the applied torque is related to the fibres' probability density function as demonstrated by Doi & Edwards (1989). First a potential is formed from the probability density function as

$$\mathscr{U} = k_B T \ln [P(\boldsymbol{x}_c, \boldsymbol{p})] \tag{2.24}$$

where k_B is Boltzmann's constant and T is the absolute temperature. The Brownian torque is proportional to a gradient of this potential in orientation space (Doi & Edwards 1989):

$$\mathscr{N}_i = -\epsilon_{ijk}\, p_j \frac{\partial \mathscr{U}}{\partial p_k}. \tag{2.25}$$

In order to test the nonlocal extra stress derived in equation (2.19) comparisons can be made to existing theories for the extra stress in unbound suspensions of rigid particles. Earlier works (Hinch & Leal 1972, 1975, 1976) assumed a constant velocity gradient within the suspension and a homogeneous particle distribution. Considering the fibres to be distributed randomly with respect to their centre of masses and assuming that the suspension is not bounded, the probability density function which has units of number density becomes a constant number density multiplying an orientation distribution function. Specifically,

$$\lim P(z, \theta, \phi) \to n\Phi(\theta, \phi) \tag{2.26}$$

where $\Phi(\theta, \phi)$ is the fibres' orientation distribution function. Applying the assumptions of constant velocity gradient, random fibre centre-of-mass placement and no suspension boundaries to the extra stress defined by equation (2.19) while neglecting Brownian motion, one can analytically derive the deviatoric extra stress,

$$\sigma'_{ij} = \frac{8\pi n \ell^3}{3 \ln [2/\varepsilon]} \left\{ \langle p_i p_j p_k p_l \rangle - \tfrac{1}{3} \delta_{ij} \langle p_k\, p_l \rangle \right\} \frac{\partial u_k}{\partial x_l}, \tag{2.27}$$

where the brackets, $\langle \cdot \rangle$, denote averages over the fibres' orientation distribution function. This form of the extra stress agrees with earlier work by Batchelor (1970) and exactly reproduces the results of Hinch & Leal (1972, 1975, 1976).

Assuming that the fibres' orientation distribution function arises from a consideration of Brownian motion within the suspension, the distribution function can be used to calculate Brownian stresses. Using equation (2.26) to relate the orientation distribution function to the probability density, the Brownian torques on the suspended fibres can be calculated by substituting equation (2.26) in equations (2.25) and (2.24). Substituting this Brownian torque into the body torque term of the extra stress, the last term in equation (2.19), and simplifying using Green's theorem for a closed spherical surface (Berry & Russel 1987), one can derive the Brownian contribution to the extra stress for an unbound suspension of fibres. The Brownian contribution to the extra stress that we derive in this manner, viz.

$$\sigma'_{ij} = n k_B T \left(3 \langle p_i\, p_j \rangle - \delta_{ij} \right), \tag{2.28}$$

is identical to the result of Hinch & Leal (1972, 1975, 1976) for an unbound suspension of non-spherical particles. Thus, the nonlocal extra stress recovers the local extra stress relationships when the nonlocal elements of the problem are removed.

Finally, equations (2.19), (2.20), (2.21), (2.24) and (2.25) complete the description of

the nonlocal average extra stress. However this system of equations leaves the extra stress in terms of a probability density function and a velocity field. To continue the development we derive the governing equations for the probability density function in the next section.

3. The governing probability density equation

Assuming that the suspended fibres collide with solvent molecules frequently enough such that the collisions produce a random, fluctuating force on the fibres, and that this force is independent of fibre motion, a Fokker–Planck governing equation applies to the fibres' probability density function; (i.e. Chandrasekhar 1943; Doi & Edwards 1989; McQuarrie 1976). Because the rigid fibres are elongated and freely suspended, they can translate and rotate about their centre of mass. The governing Fokker–Planck equation for particles free to translate and rotate is (Brenner 1974; Chandrasekhar 1943; McQuarrie 1976)

$$\frac{\partial P}{\partial t} + \frac{\partial j_i^x}{\partial x_i} + \frac{\partial j_i^p}{\partial p_i} = 0, \tag{3.1}$$

where $\partial/\partial x_i$ and $\partial/\partial p_i$ are gradients in translational and orientational space respectively. Accordingly, the terms j_i^x and j_i^p are fluxes of probability in translational and rotational space. Equation (3.1) represents a simple conservation law wherein any change in the probability density must be balanced by the divergence of the fluxes in translational and rotational space. These probability fluxes are defined as

$$j_i^x = U_i P - D_{ij}\frac{\partial P}{\partial x_j}, \tag{3.2}$$

$$j_i^p = \dot{p}_i P - d_{ij}\frac{\partial P}{\partial p_j} \tag{3.3}$$

where U_i is the translational velocity and $\dot{p}_i$ the rotational velocity of a fibre with respect to its centre of mass. The translational and rotational diffusion tensors are represented by D_{ij} and d_{ij} respectively. Coupling between a fibre's rotational and translational motion is ignored because the slender fibres we consider lack the geometric features to couple these processes (Brenner 1974; Nitsche 1991; Nitsche & Brenner 1990), i.e. they have no twist or curvature.

To simplify the governing probability equations we consider the coordinate geometry pictured in figure 3. Thus, confining the suspension of fibres between two infinite parallel plates where the coordinate system is chosen to lie on the lower plate with the x_3 axis pointing towards the upper plate, fluid flow is unidirectional in the x_2 direction making x_1 the vorticity axis while implying that P is independent of x_2. By moving the upper plate while holding the lower plate fixed, shear flow is imposed, while fixing both plates and applying a pressure gradient in the x_2 direction creates plane Poiseuille flow. The gap width h is made dimensionless with the fibre half-length, ℓ and denoted as λ. In this geometry, a fibre's centre-of-mass distance from the lower wall is z (where z has been made dimensionless with ℓ as $z = x_3/\ell$). Two rotation angles, θ and ϕ, determine a fibre's orientation where θ is the angle the fibre's major axis makes with the normal to the lower wall and ϕ is the angle that the projection of the fibre's major axis onto the (x_1, x_2)-plane makes with the x_1 axis. Defined as such, θ and ϕ are identical to angular ordinates in a spherical coordinate system (Marion & Thornton 1988). Complete specification of a fibre's

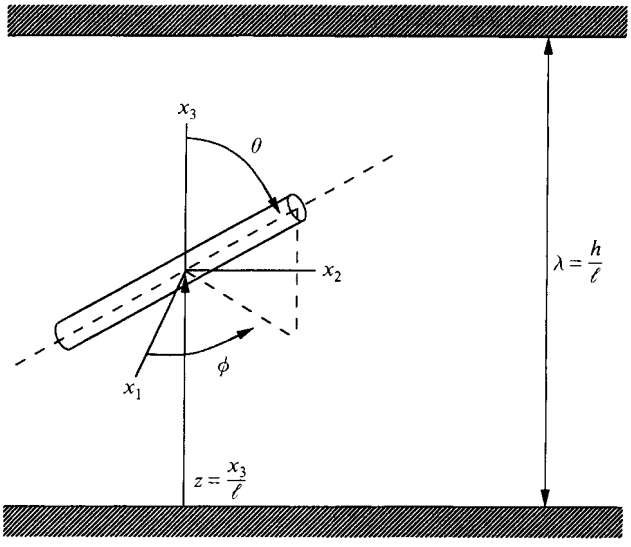

FIGURE 3. Problem geometry and notation.

configuration is therefore given by its centre-of-mass position and two orientation angles.

Translational and rotational diffusion tensors for a slender fibre in an unbound suspension are defined as

$$D_{ij} = p_i p_j D_{\parallel} + (\delta_{ij} - p_i p_j) D_{\perp}, \tag{3.4}$$

$$d_{ij} = (\delta_{ij} - p_i p_j) D_r, \tag{3.5}$$

where $D_{\parallel}$ is the translational diffusivity for a rod moving parallel to its major axis, $D_{\perp}$ is the translational diffusivity for a rod moving perpendicular to its major axis and D_r is the rotary diffusivity for a rod rotating about its centre of mass. Changes in a fibre's mobility and thus its diffusion tensors due to interactions with surrounding boundaries or other fibres are ignored in our derivation to simplify the governing equations. There is evidence, moreover, that neglecting a fibre's hydrodynamic mobility change as it approaches a wall is a very reasonable approximation. Experimental work of Russel *et al.* (1977) found that the sedimentation velocity of a fibre falling near a wall is unaffected by the wall provided that the fibre–wall separation is greater than one fibre half-length. When the fibre–wall separation is less than a fibre half-length, translational motion perpendicular to the wall is weakly affected while translational motion parallel to the wall remains unaffected within their experimental error (Russel *et al.* 1977). Additionally, one can consider changes in a fibre's hydrodynamic mobility due to the presence of other fibres in the suspension. As reported by Doi & Edwards (1989), a fibre's rotational diffusivity is approximately constant for $n\ell^3 \leqslant 4$. While changes in a fibre's mobility are neglected, the fluid boundaries rigorously impose a zero particle flux condition which will be presented later in this section. Neglecting changes in a fibre's mobility in no way implies that at the fluid boundaries the no flux condition is ignored. Rather, assuming constant mobilities is a simplification that is well justified for dilute suspensions.

Combining equations (3.1)–(3.5) and simplifying yields

$$\kappa^2 \left[1 - \rho \sin^2\theta\right] \frac{\partial^2 P}{\partial z^2} + \frac{1}{\sin\theta} \frac{\partial}{\partial\theta} \left[\sin\theta \frac{\partial P}{\partial\theta}\right] + \frac{1}{\sin^2\theta} \frac{\partial^2 P}{\partial\phi^2}$$
$$= Pe \left\{ \frac{1}{\sin\theta} \frac{\partial}{\partial\theta} \left[\sin\theta \cos\theta \sin\phi \, g(z,\theta) P\right] + \frac{1}{\sin\theta} \frac{\partial}{\partial\phi} \left[\cos\phi \, g(z,\theta) P\right] \right\} \quad (3.6)$$

with the following definitions:

$$g(z,\theta) = \frac{3}{2} \int_{-1}^{+1} s \langle u_2 \rangle (z + s\cos\theta) \, \mathrm{d}s, \quad (3.7)$$

$$Pe = \frac{\dot{\gamma}}{D_r}, \quad (3.8)$$

$$\kappa^2 = \frac{D_\parallel}{\ell^2 D_r} = \frac{2}{3} \qquad \text{for slender fibres,} \quad (3.9)$$

$$\rho = 1 - \frac{D_\perp}{D_\parallel} = \frac{1}{2} \qquad \text{for slender fibres.} \quad (3.10)$$

In the above equations all lengths have been made dimensionless with the fibre half-length ℓ. Velocity has been made dimensionless with $\dot{\gamma}\ell$ in equation (3.13) where $\dot{\gamma}$ is the bulk applied shear rate for simple shear flows or the shear rate at the wall for pressure-driven flows. The scalar ratios κ^2 and ρ of the diffusion coefficients are constant for slender bodies (Batchelor 1970). This non-dimensionalization of the governing probability equations is consistent with earlier work by Nitsche (1991).

Equation (3.6) represents a balance between diffusive and convective flux of the probability density function, a balance which is controlled by the value of the rotary Péclet number, Pe, defined here as the ratio of the bulk shear rate $\dot{\gamma}$ to the rotary diffusivity D_r. Under the condition of strong Brownian motion, or weak flow, diffusive motion will dominate and $Pe \ll 1$. We shall be concerned with this asymptotic limit since in this parameter regime significant Brownian stresses can develop, and moreover, Brownian forces tend to orient particles away from the flow direction thus creating large hydrodynamic stresses. It follows that the largest stresses in fibre suspensions are found for flows near equilibrium. It is these large extra stresses and their variation under nonlocal conditions that we shall primarily investigate.

As a second-order partial differential equation in z, θ and ϕ, the governing equation for the probability density function, equation (3.6), requires six boundary conditions for solution. Four boundary conditions arise from the zero particle flux constraint applied at the walls. For spherical particles the no-flux constraint implies that at a boundary the translational flux j_i^x normal to that boundary is zero. A similar condition applies to the probability density function $P(z,\theta,\phi)$ but now the surface on which the normal component of the flux vanishes is more complicated. In the set of all phase-space points for this system (z,θ,ϕ), there is a subset of allowed configurations and its complement, a set of forbidden configurations. For a bound suspension of fibres, forbidden configurations correspond to positions and orientations that place any fibre within the walls. Separating these sets is a hypersurface, and the local normal to this surface when dotted into the rotational and translational probability flux must be zero. Explicitly this implies

$$n_i^s \left(j_i^x + j_i^p\right) = 0, \quad (3.11)$$

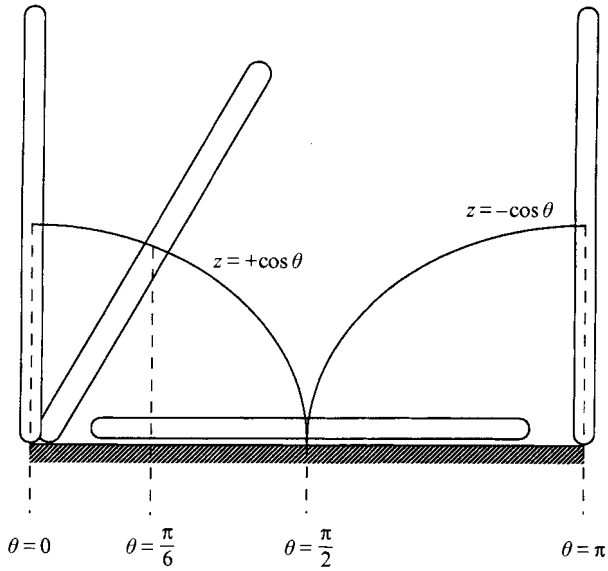

FIGURE 4. Geometric constraints on a fibre near a boundary.

where n_i^s is the local normal to the hypersurface separating allowed and forbidden configurations. Simplifying equation (3.11) for the geometry used in figure 3 yields

$$-\kappa^2\left[1-\rho\sin^2\theta\right]\frac{\partial P}{\partial z} \pm \sin\theta\left(Pe\cos\theta\sin\phi\, g(z,\theta,\phi)\; P - \frac{\partial P}{\partial\theta}\right) = 0 \quad \text{on } z = \pm\cos\theta \qquad (3.12)$$

for the lower boundary at $z = 0$, and the following for the upper boundary at $z = \lambda$:

$$-\kappa^2\left[1-\rho\sin^2\theta\right]\frac{\partial P}{\partial z} \mp \sin\theta\left(Pe\cos\theta\sin\phi\, g(z,\theta,\phi)\; P - \frac{\partial P}{\partial\theta}\right) = 0 \quad \text{on } z = \lambda \mp \cos\theta. \qquad (3.13)$$

In equations (3.12) and (3.13) the upper sign is used when $0 \leqslant \theta \leqslant \pi/2$ and the lower sign is used when $\pi/2 \leqslant \theta \leqslant \pi$. This form for the no-flux boundary condition is consistent with the earlier works (Nitsche & Brenner 1990; Nitsche 1991).

The no-flux constraints embodied in equations 3.12 and 3.13 state that for a fibre in contact with a wall, translational and rotational motions must be coupled to prevent the fibre from rotating or translating through that wall. As shown graphically in figure 4, for a fibre in contact with the wall a negative flux in the z-direction (motion of the centre of mass towards the wall) must be coupled by positive flux in the θ-direction (rotation keeping the end of fibre from penetrating the wall). In moving from $\theta = 0$ to $\theta = \pi/6$, a positive θ flux, the fibre in figure 4 moves its centre of mass closer to the wall undergoing a negative z flux. This coupling of translational and rotational motion explains the necessity of the coupled no-flux condition and the sign requirements balancing each term in equations (3.12) and (3.13).

Together the no-flux constraints on the upper and lower walls place four boundary conditions on the probability density function, one constraint on z and one on θ for each equation. Rotation of a fibre in the ϕ-direction cannot move the fibre through a wall, cf. figure 3. Thus, it is consistent that the no-flux conditions must hold for all ϕ and not place any restrictions on a fibre's orientation in that angle. Since the

probability density function must be finite and continuous for all allowed z, θ and ϕ, it must be periodic in ϕ. This periodicity condition implies

$$P(z, \theta, \phi + 2\pi) = P(z, \theta, \phi). \tag{3.14}$$

Physically, since the geometry of our system as shown in figure 3 is symmetric with respect to the flow–velocity gradient plane (the x_2, x_3 plane), the probability density function or distribution of fibres within the suspension must by symmetric about this plane as well. To produce this symmetry, the probability density function must be periodic in ϕ.

In addition to the no-flux and periodicity requirements, a final boundary condition must be placed on the probability density function to ensure that it is mathematically unique. The final constraint is normalization such that upon integration over all allowed configurations in some volume V of the suspension, the probability density must equal the number of fibres within that volume. This normalization requires

$$\int_V \mathrm{d}V \int_{\theta_1(z)}^{\theta_2(z)} \mathrm{d}\theta \int_0^{2\pi} \mathrm{d}\phi \, P(z, \theta, \phi) \sin\theta = N \tag{3.15}$$

where N is the total number of fibres within the volume V and the functions $\theta_1(z)$ and $\theta_2(z)$ refer to the minimum and maximum allowed angles in the θ-direction for a given z-position. For the geometry shown in figure 3, θ_1 and θ_2 are defined as

$$\theta_1 = \begin{cases} 0 & \text{for } z \geqslant 1 \text{ and } z \leqslant (\lambda - 1) \\ \arccos(z) & \text{for } z \leqslant 1, \\ \arccos(\lambda - z) & \text{for } z \geqslant (\lambda - 1), \end{cases} \tag{3.16}$$

and

$$\theta_2 = \begin{cases} \pi & \text{for } z \geqslant 1 \text{ and } z \leqslant (\lambda - 1) \\ \arccos(-z) & \text{for } z \leqslant 1. \\ \arccos(-\lambda + z) & \text{for } z \geqslant (\lambda - 1). \end{cases} \tag{3.17}$$

Since the system we consider is invariant to translation in the x_1- and x_2-directions the volume integral in the normalization condition, equation (3.15), can be completed over a cross-section in the (x_1, x_2) plane. Denoting the area of this cross-section as A_{12}, the normalization constraint becomes

$$\int \mathrm{d}x_1 \int \mathrm{d}x_2 \int \mathrm{d}x_3 \int_{\theta_1(x_3)}^{\theta_2(x_3)} \mathrm{d}\theta \int_0^{2\pi} \mathrm{d}\phi \, P(x_3, \theta, \phi) \sin\theta \tag{3.18}$$

$$= A_{12}\ell \int_0^{\lambda} \mathrm{d}z \int_{\theta_1(z)}^{\theta_2(z)} \mathrm{d}\theta \int_0^{2\pi} \mathrm{d}\phi \, P(z, \theta, \phi) \sin\theta = N. \tag{3.19}$$

In moving from equation (3.18) to equation (3.19) the differential element $\mathrm{d}x_3$ has been made dimensionless with fibre half-length ℓ as $\mathrm{d}x_3 = \ell \mathrm{d}z$ and the integration domain in the z-direction has been set to the entire gap width. This moves the volume dimensionality to the quantity $A_{12}\lambda\ell$ such that when transferred to the right-hand side of equation (3.19) the normalization condition becomes

$$\int \mathrm{d}z \int_{\theta_1(z)}^{\theta_2(z)} \mathrm{d}\theta \int_0^{2\pi} \mathrm{d}\phi \, P(z, \theta, \phi) \sin\theta = \frac{N\lambda}{A_{12}\lambda\ell} = n\lambda. \tag{3.20}$$

Since the domain of integration in the z-direction is the entire gap from $z = 0$ to λ, the number density n in equation (3.20) corresponds to the number density of fibres within the confined suspension.

At this point it is useful to consider the physical implications involved in normalizing the probability density function through equation (3.20). Conceptually, the normalization represented in equation (3.20) implies that the sum of the probability density over all configuration states must equal the number density times λ. In an unbound suspension, the meaning of the number density is unique and simple; n is the number of fibres per unit volume of the suspension. However, in a bound suspension the meaning of the number density is more complicated, and can be defined in two distinct ways. The simplest way to understand the two different interpretations of the number density is through consideration of two experiments. In the first experiment, a fluid of volume V containing N fibres is placed between two infinite, parallel plates separated by a distance λ. If the fibres were allowed to freely rotate near the boundaries, but could not pass their centre-of-mass through these boundaries, then the number density of fibres in the confined suspension would simply be $n = N/V$. However, fibres cannot freely rotate through a solid boundary, and near a solid boundary there is a reduced set of centre of mass positions, z, and orientations, θ, available to the fibres as expressed in equations (3.16) and (3.17). Since the N fibres in the confined suspension are constricted to a reduced set of centre-of-mass positions and orientations, they are restricted to a fractionally smaller volume than the volume available to the supporting fluid. Therefore, the number density of fibres, n, in the volume available to the confined suspension is greater than N/V. The degree to which the fibre number density is greater than N/V can be determined by satisfying the normalization condition, equation (3.20), in the absence of flow.

Under quiescent, equilibrium conditions, the probability density is uniform and constant within *all allowed configurations*. Thus in the absence of flow, the probability density function has the form

$$P(z, \theta, \phi) = \frac{N M(\lambda)}{V} = n M(\lambda) \tag{3.21}$$

where $M(\lambda)$ is a normalization constant that will depend on total gap width, λ. Substituting this probability density into the normalization constraint, equation (3.20), and conducting the integration while observing the restriction in allowed fibre orientations, equations (3.16) and (3.17) determine the normalization constant as

$$M(\lambda) = \begin{cases} \dfrac{1}{\pi\lambda} & \text{for } \lambda \leqslant 2 \\ \dfrac{\lambda}{4\pi(\lambda - 1)} & \text{for } \lambda \geqslant 2. \end{cases} \tag{3.22}$$

Physically the normalization scaling of $1/\lambda$ and $\lambda/(\lambda - 1)$ results from a steric depletion of allowed fibre configurations near the boundaries. In a gap of width λ and cross-sectional area A, a volume smaller than $A\lambda$ is available to the fibres. This reduction in available volume causes the local concentration of fibres to be fractionally larger for a bound suspension compared to an unbound suspension. If a fluid with number density n fibres per unit volume is placed between two parallel plates infinitely far apart, then the local concentration of fibres remains n. However, as the plates are brought towards each other the effective number density increases as $n_{eff} = n\lambda/(\lambda - 1)$ for $\lambda \geqslant 2$ reflecting the fact that within the available configurational states for fibres the effective number density has increased over the bulk. Hereafter we will refer to this normalization as a normalization for a reduced available volume.

The second interpretation of the number density in a bound suspension can be understood by considering the following experiment. Consider a slightly different system from the one described above where a fluid between two parallel plates is in equilibrium with an unbound reservoir of fluid, then the number density of fibres within the reservoir and within the available states between the parallel plates would be the same.

At equilibrium, there is a difference in the chemical potential between the fibres in the gap and the fibres in the reservoir. Ignoring hydrodynamic and electrostatic interactions between the fibres and the walls, an energy balance combined with the definition of the chemical potential (McQuarrie 1976) shows that the difference in the chemical potential between bound and unbound fibres is equal to the ratio of the accessible volume within the gap to the total volume within the gap. Within the available states the chemical potential of fibres in the gap and in the reservoir is the same, and thus so is the fibre concentration within the available states. Considering the total volume of the gap, the chemical potential difference scales as $4/\lambda$ for $\lambda \leqslant 2$ and $\lambda/(\lambda - 1)$ for $\lambda \geqslant 2$.

To consider our model problem and results in this work as a confined suspension in equilibrium with an unbound bulk suspension, all that need be done is replace the normalization constant, $M(\lambda)$, with $1/(4\pi)$. Hereafter, whenever this replacement is done, we will refer to it as normalized for equilibrium with an unbound suspension. Often it is easier to understand our results under this normalization since a suspension of fibres with number density n will remain at that concentration regardless of the gap width whereas when normalized for reduced available volume, the true number density will change as the gap width is varied.

Together the equations (3.6), (3.7), (3.12), (3.13), (3.14) and (3.20) completely specify the fibres' probability density function. However, this specification leaves the probability density coupled with the fluid velocity field through the term $g(z, \theta)$ as defined in equation (3.7). In the next section, the governing equations for the fluid are derived which will complete the mathematical description of the extra stress of the previous section and the probability density function of this section.

4. Average momentum equations for the suspension

Derivation of the equations governing the motion begins with a momentum balance on a volume of the suspension at steady state. We consider a volume in which the fibres are experiencing a net force and torque. From superposition we can combine the nonlocal extra stress derived in §2 where the fibres were subjected to an external torque with the averaged momentum equations derived in this section to describe a suspension of fibres experiencing both external torques and forces. If a volume of suspension containing fibres is experiencing a net body force then Cauchy's equation for the fluid is

$$\frac{\partial \sigma_{ij}}{\partial x_j} = F_i \tag{4.1}$$

where F_i is the force density on the fibres in the suspension assuming the fluid is force free. Substituting the total stress defined in equation (2.1) into the above expression and ensemble averaging over all configurations of fibres within the suspension yields

$$\mu \frac{\partial^2 \langle u_j \rangle}{\partial x_i \partial x_j} + \frac{\partial \langle \sigma'_{ij} \rangle}{\partial x_j} - \frac{\partial \langle \mathscr{P} \rangle}{\partial x_i} = \langle F_i \rangle . \tag{4.2}$$

As before, u_j represents the fluid velocity and $\mathscr{P}$ is the fluid pressure. The ensemble-averaged force density in equation (4.2) is by definition of an ensemble average (McQuarrie 1976)

$$\langle F_i \rangle (\boldsymbol{x}) = \int_{\Omega} \mathrm{d}\boldsymbol{p} \int_{\boldsymbol{x} \in D(\boldsymbol{x}_c, \boldsymbol{p})} \mathrm{d}\boldsymbol{x}_c \left\langle F_i \left(\boldsymbol{x} | \boldsymbol{x}_c, \boldsymbol{p}\right) \right\rangle_1 P \left(\boldsymbol{x}_c, \boldsymbol{p}\right). \tag{4.3}$$

As with the extra stress, the force density is approximately constant over displacements of $O(b)$ perpendicular to the fibre's central axis. Thus, the first conditionally averaged force density, $\left\langle F_i \left(\boldsymbol{x} | \boldsymbol{x}_c, \boldsymbol{p}\right) \right\rangle_1$, can be integrated over the cross-section of a fibre yielding

$$\langle \overline{F}_i \rangle (\boldsymbol{x}) = \int_{\Omega} \mathrm{d}\boldsymbol{p} \int_{-\ell}^{+\ell} \mathrm{d}s \left\langle \overline{F}_i \left(\boldsymbol{x} | \boldsymbol{x} - s\boldsymbol{p}, \boldsymbol{p}\right) \right\rangle_1 P \left(\boldsymbol{x} - s\boldsymbol{p}, \boldsymbol{p}\right). \tag{4.4}$$

On integration over a cross-section of a fibre, the force density, F_i, becomes a force per unit length denoted as $\overline{F}_i$.

To relate the force per unit length to a body force felt by the fibres, consider a fixed fibre with a force per unit length of $f_i(s)$ at some cross-section s where the total force on the fibre is $\mathscr{F}_i$. If the body force results from a continuous, uniformly distributed force density throughout the fibre, a force balance on a section of that fibre from one end where $s = -\ell$ to a general cross-section s, requires that

$$\int_{-\ell}^{s} \mathrm{d}\hat{s} f_i \left(\hat{s} | \boldsymbol{x}_c, \boldsymbol{p}\right) = (s + \ell) f_i \left(\hat{s} | \boldsymbol{x}_c, \boldsymbol{p}\right) = \frac{(s+\ell)}{2\ell} \mathscr{F}_i (\boldsymbol{x}_c, \boldsymbol{p}). \tag{4.5}$$

Equation (4.5) states that the body force is evenly distributed over the length of a fibre and depends only on its centre-of-mass position and orientation. For a large aspect ratio body, the force per unit length of equation (4.4) is related to the total force shown in equation (4.5) through

$$\overline{F}_i \left(s | \boldsymbol{x}_c, \boldsymbol{p}\right) = \frac{1}{2\ell} \mathscr{F}_i (\boldsymbol{x}_c, \boldsymbol{p}). \tag{4.6}$$

Combining the relationship between the force densities, equation (4.6), with the ensemble-averaged force density relation, equation (4.4), completes the definition of the ensemble-averaged force per unit length

$$\langle \overline{F}_i \rangle (\boldsymbol{x}) = \int_{\Omega} \mathrm{d}\boldsymbol{p} \int_{-\ell}^{+\ell} \mathrm{d}s \left(\frac{1}{2\ell}\right) \mathscr{F}_i (\boldsymbol{x} - s\boldsymbol{p}, \boldsymbol{p}) P \left(\boldsymbol{x} - s\boldsymbol{p}, \boldsymbol{p}\right). \tag{4.7}$$

Substituting the force density relationship derived in equation (4.7) into the governing momentum balance equation (4.2) one arrives at the governing nonlocal momentum equation

$$\mu \frac{\partial^2 \langle u_j \rangle}{\partial x_i \partial x_j} + \frac{\partial \langle \sigma'_{ij} \rangle}{\partial x_j} - \frac{\partial \langle \mathscr{P} \rangle}{\partial x_i} = \int_{\Omega} \mathrm{d}\boldsymbol{p} \int_{-\ell}^{+\ell} \mathrm{d}s \left(\frac{1}{2\ell}\right) \mathscr{F}_i (\boldsymbol{x} - s\boldsymbol{p}, \boldsymbol{p}) P \left(\boldsymbol{x} - s\boldsymbol{p}, \boldsymbol{p}\right). \tag{4.8}$$

Finally, for the problem under consideration, the body force term, $\mathscr{F}_i$ is related to a Brownian force as shown by Chandrasekhar (1943), Doi & Edwards (1989) and Larson (1988). As with the Brownian torque in §2, the Brownian force is proportional to a gradient of a potential which depends on a probability density function as in equation (2.24), viz.

$$\mathscr{F}_i = -\frac{\partial \mathscr{U}}{\partial x_{ci}}. \tag{4.9}$$

Substituting the definition of the potential from equation (2.24) into equations (4.9)

and (4.8), one finds that the body force integral in the momentum balance can be expressed as a gradient of a scalar function. Thus, the integral of the body force term in equation (4.8) can be written

$$\int_\Omega \mathrm{d}\boldsymbol{p} \int_{-\ell}^{+\ell} \mathrm{d}s \left(\frac{1}{2\ell}\right) \mathscr{F}_i(\boldsymbol{x} - s\boldsymbol{p}, \boldsymbol{p})\, P(\boldsymbol{x}_c, \boldsymbol{p}) = \frac{\partial}{\partial x_i}\left[-k_B T \int_\Omega \mathrm{d}\boldsymbol{p} \int_{-\ell}^{+\ell} \mathrm{d}s \left(\frac{1}{2\ell}\right) P(\boldsymbol{x} - s\boldsymbol{p}, \boldsymbol{p})\right]. \tag{4.10}$$

The nonlocal body force term in the governing momentum balance behaves as an osmotic pressure where the term in brackets is the scalar function representing the extra pressure due to body force acting on the suspended fibres. Derivation of a thermodynamic pressure in a suspension from a momentum balance was shown by Brady (1993) to be equivalent to an osmotic pressure. The total extra pressure, or osmotic pressure due to the fibres, is the sum of the above body force contribution and the trace of the extra stress derived in §2.

Equations (4.8) and (4.10) complete the derivation of the governing momentum balance and couple this balance to the extra stress derived in §2 and the probability density function derived in §3. The methods used to solve this coupled set of equations and thus determine the rheology in shear and pressure-driven flow are discussed in the next section.

5. Solution techniques

Equations (2.19)–(2.21), (2.24), (2.25), (3.6)–(3.10), (3.12)–(3.14), (3.20), (4.8)–(4.10) completely specify an ensemble-averaged extra stress, average velocity field and probability density function for rigid slender fibres confined between two parallel plates. To solve this set of coupled, nonlinear integral-differential equations under conditions of weak flow, or strong Brownian motion, a series solution in powers of the small parameter, the Péclet number, is sought. Expanding the extra stress, velocity and probability density in terms of the Péclet number we obtain

$$\langle \sigma_{ij} \rangle = \langle \sigma_{ij} \rangle^{(0)} + Pe\, \langle \sigma_{ij} \rangle^{(1)} + Pe^2\, \langle \sigma_{ij} \rangle^{(2)} + \cdots, \tag{5.1}$$

$$\langle u_2 \rangle = \langle u_2 \rangle^{(0)} + Pe\, \langle u_2 \rangle^{(1)} + Pe^2\, \langle u_2 \rangle^{(2)} + \cdots, \tag{5.2}$$

$$P = P^{(0)} + Pe\, P^{(1)} + Pe^2\, P^{(2)} + \cdots. \tag{5.3}$$

Substitution of this series expansion into the governing equations and equating like powers of Pe removes the nonlinearities resulting from products of velocity and probability by separating these terms to different orders in the Péclet number.

While the expansion in Péclet number separates the nonlinear terms, the overall system remains coupled at finite fibre concentrations because calculation of the extra stress requires the probability density function and velocity field, which will deviate significantly from those in purely Newtonian flows. However, in the limit of zero fibre concentration, the velocity field is that of a Newtonian fluid and one can directly calculate the probability density function using known techniques (Bird & Warner 1971; Brenner 1974; Brunn 1976; Brunn & Grisafi 1987; Nitsche 1991; Nitsche & Brenner 1990; Stewart & Sorensen 1972). From this probability density function, the extra stress profiles to first order in concentration can be calculated. However, these calculated stress profiles are only valid in the limit of vanishingly small concentration, i.e. $n\ell^3 \to 0$. Though this limitation is restrictive,

these results are not without value in that they are simple to construct and provide a useful check on the fully self-consistent calculations discussed below. We shall return to these asymptotic solutions for small concentration in §6.1.

Considering the entire set of governing equations, one can solve for the extra stress, velocity and probability density simultaneously providing fully self-consistent results. These self-consistent calculations are valid for finite fibre concentrations in that the fibres and their extra stress affect the mean flow which, in turn, affects the value of the stress contribution for each fibre. However, within these approximations, the fibres only interact through the mean flow.

To solve the system of equations (2.19)–(2.21), (2.24), (2.25), (3.6)–(3.10), (3.12)–(3.14), (3.20), (4.8)–(4.10), we note that the velocity and extra stress depend on position within the gap z while the probability depends on three-variables, z, θ and ϕ. Solution of this fully three dimensional problem is a formidable task analytically or numerically. However, our choice of coordinate system used allows a reduction in the dimension of the system by one. As shown in figure 3, the orientation angle ϕ describes the fibre's orientation relative to the vorticity axis which is perpendicular to the flow. Since the fluid boundaries are parallel to the flow and the vorticity axis, rotation in the ϕ-direction cannot force a fibre through a boundary. Though it appears in the no-flux boundary conditions, equations (3.12) and (3.13), the angle ϕ can have any value and the no-flux conditions must still hold. This suggests that like the governing equation for the probability density function, equation (3.6), the no-flux boundary conditions are separable in the variable ϕ at every order in the Péclet number expansion.

Applying separation of variables on the governing equations to remove the ϕ-dependence, and applying the constraint that the solution be periodic in ϕ, the probability density function to second order in Pe has the form

$$P(z,\theta,\phi) = n\,M(\lambda)\left\{1 + Pe\sin\phi\,\mathscr{H}(z,\theta) + Pe^2\left[\mathscr{G}_1(z,\theta) - \cos 2\phi\,\mathscr{G}_2(z,\theta)\right]\right\}. \quad (5.4)$$

In equation (5.4), $M(\lambda)$ refers to the normalization constant determined by equation (3.20) and n is the fibre number density. The terms $\mathscr{H}(z,\theta)$, $\mathscr{G}_1(z,\theta)$ and $\mathscr{G}_2(z,\theta)$ refer to unknown functions of z and θ. This form for the probability density function agrees with earlier works of Bird & Warner (1971) and Stewart & Sorensen (1972) once the coordinate system is rotated to move the shear plane from the $(y,\ z)$ plane to their choice of shear in the $(x,\ y)$ plane.

Substituting the general probability density function of equation (5.4) into the normalization condition, equation (3.20) allows analytic calculation of the normalization term, $M(\lambda)$. The normalization function is

$$M(\lambda) = \begin{cases} \dfrac{1}{\pi\lambda + O(Pe^2)} & \text{for } \lambda \leqslant 2 \\ \dfrac{\lambda}{4\pi(\lambda-1) + O(Pe^2)} & \text{for } \lambda \geqslant 2. \end{cases} \quad (5.5)$$

Once $\mathscr{G}_1$ and $\mathscr{G}_2$ are determined, the numeric coefficients on the Pe^2 terms can be calculated and are $\frac{183}{3840}$ and $\frac{193}{3840}$ for $\lambda \leqslant 2$ and $\lambda \geqslant 2$ respectively. As was discussed in §3, the normalization in equation (5.5) is a normalization for a reduced available volume. Since the geometry considered in this work is a fluid confined between two infinite, parallel plates with finite separation, we will proceed with normalization of the problem for a reduced available volume throughout this work, except where noted.

Since the ϕ-functionality in the probability density function and the normalization

function are known, it follows that to determine the extra stress, velocity field and probability density function, one must solve simultaneously a one-dimensional problem for the extra stress and fluid velocity and a two-dimensional problem for the probability density function (or rather its constituent parts $\mathscr{H}(z,\theta)$, $\mathscr{G}_1(z,\theta)$ and $\mathscr{G}_2(z,\theta)$). Moreover, we note that since $O(Pe^1)$ terms in the probability density function contribute to the $O(Pe^0)$ Brownian torque and force terms in the extra stress and momentum balance, one can solve to $O(Pe^0)$ in extra stress and velocity while only solving the probability density function problem to $O(Pe^1)$. Once that problem is completed, one can then solve the $O(Pe^1)$ problem for extra stress and velocity while simultaneously solving the $O(Pe^2)$ problem in probability. Thus the system has been reduced to first solving two one-dimensional problems for $\langle\sigma_{ij}\rangle^{(0)}(z)$ and $\langle u_2\rangle^{(0)}(z)$ and a two-dimensional problem for $\mathscr{H}(z,\theta)$ simultaneously, followed by solving again two one-dimensional problems for $\langle\sigma_{ij}\rangle^{(1)}(z)$ and $\langle u_2\rangle^{(1)}(z)$ and two two-dimensional problems for $\mathscr{G}_1(z,\theta)$ and $\mathscr{G}_2(z,\theta)$. Though this solution method is still difficult, the dimensional order of the problem has been reduced, and the results for the probability density function can be compared to earlier works (Bird & Warner 1971; Stewart & Sorensen 1972) in the limit as the gap width $\lambda \to \infty$.

After the problem has been reduced to solving a series of one- and two-dimensional problems simultaneously, solution of the reduced system proceeds in several different ways. In the limit of very small gaps, $\lambda \to 0$, fully analytic solutions are found for the governing extra stress, velocity and probability density functions. For intermediate and large gap widths, the governing equations are solved numerically using fourth-order finite differencing. The accuracy of the numerical results is checked by comparison to the analytic results in the large and small gap limits. The semi-analytic and numeric technique of boundary collocation used previously (Nitsche & Brenner 1990; Nitsche 1991) was employed for intermediate gap widths as well. However, this technique which requires building Green's function solutions to the probability density equation from its eigenfunctions and distributing these Green's functions outside the problem domain to support the boundary conditions suffered from poor convergence for most intermediate gap widths, $\lambda < 50$, considered here. Thus, this technique was abandoned and finite differences were used as the main numerical method to solve this problem. Finally, all finite difference solutions were calculated on continually finer grid sizes until the calculated results ceased to change in their first four significant figures. After applying the transformation $t = \cos\theta$ to linearize the shape of the confining boundaries in the (z,θ)-space (Nitsche & Brenner 1990; Nitsche 1991) grid points were uniformly distributed in the (z,t)-space using 3000 to 6000 grid points.

For results calculated using the solution techniques outlined above, we discuss the shear flow of a suspension of rigid fibres between parallel plates in the next section.

6. Shear flow results

Shear flow is attained by moving the upper plate with a velocity $\overline{U}$ relative to the lower plate as shown in figure 3. A nonlinear velocity profile develops due to the presence of the fibres. When no fibres are present, $n\ell^3 = 0$, linear simple shear flow is attained.

Before examining the full probability density function for fibres under simple shear, it is necessary to first consider this function in the absence of flow. Under static conditions, the rods fill the gap in all allowed positions and orientations with equal probability. Near a wall with the geometry chosen for this problem, there is a reduced set of allowed orientation angles, θ, that a fibre with centre of mass at z can have.

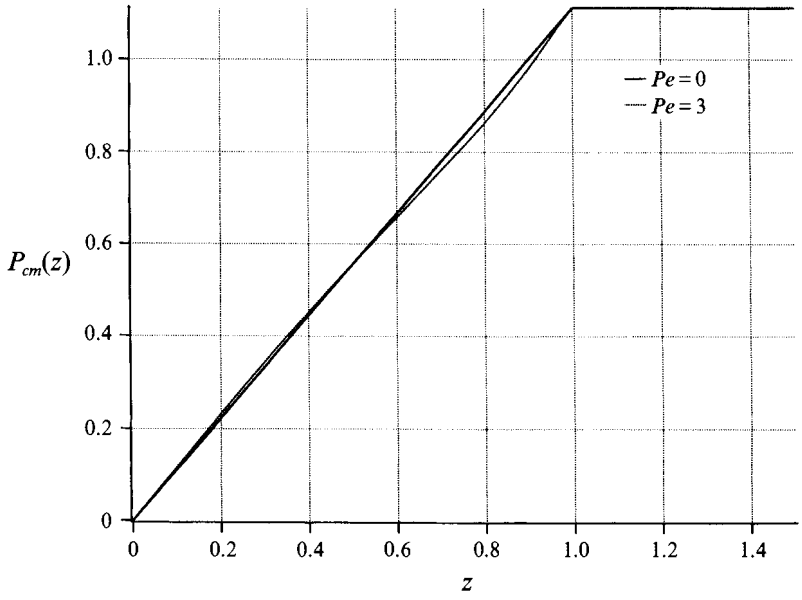

FIGURE 5. The centre-of-mass probability density function, $P_{cm}(z)$ at various shear rates: $Pe = 0$ and $Pe = 3$.

This set of angles was described earlier as θ_1 and θ_2 in equations (3.16) and (3.17), and shown graphically in figure 4. Combinations of z and θ that lie below the line $z = |\cos\theta|$ are forbidden since they necessitate the fibre passing through a wall. All combinations of z and θ above the line are allowed. Under static conditions, fibres fill all allowed configurations with equal probability.

Defining the probability of finding a fibre with its centre of mass at z as

$$P_{cm}(z) = \int_{\theta_1(z)}^{\theta_2(z)} \mathrm{d}\theta \int_0^{2\pi} \mathrm{d}\phi \sin\theta\, P(z,\theta,\phi) \tag{6.1}$$

one can calculate the centre-of-mass probability as a function of distance from the wall. Under static conditions geometric constraints cause the distribution of the probability of finding a fibre with centre-of-mass position at z to decline linearly from its constant bulk value as one approaches a wall. This behaviour in the centre-of-mass distribution has been demonstrated elsewhere for rigid rod suspensions by Magda, Tirrell & Davis (1988). Plotted in figure 5 is the centre-of-mass distribution for zero net flow, $Pe = 0$, and during flow, $Pe = 3$. The centre-of-mass probability density function is a weak function of Pe changing as $O(Pe^2)$ when flow is initiated.

For any given distance from the wall, there is a finite probability of intersecting a fibre segment from any fibre within a dimensionless distance of two from the point of interest z. Thus, one can define a segmental probability density function, or probability of intersecting a fibre segment as

$$P_{sm}(z) = \int_{z_1(z)}^{z_2(z)} \mathrm{d}z_{eff} \int_{\theta_3(z_{eff})}^{\theta_4(z_{eff})} \mathrm{d}\theta \int_0^{2\pi} \mathrm{d}\phi \sin\theta\, P(z_{eff},\theta,\phi). \tag{6.2}$$

In this definition, $z_1(z)$ and $z_2(z)$ are the minimum and maximum centre-of-mass positions within the allowed configuration space from which fibres can intersect the point of interest z. In the bulk, $z_1(z) = z - 1$ and $z_2(z) = z + 1$ since fibres

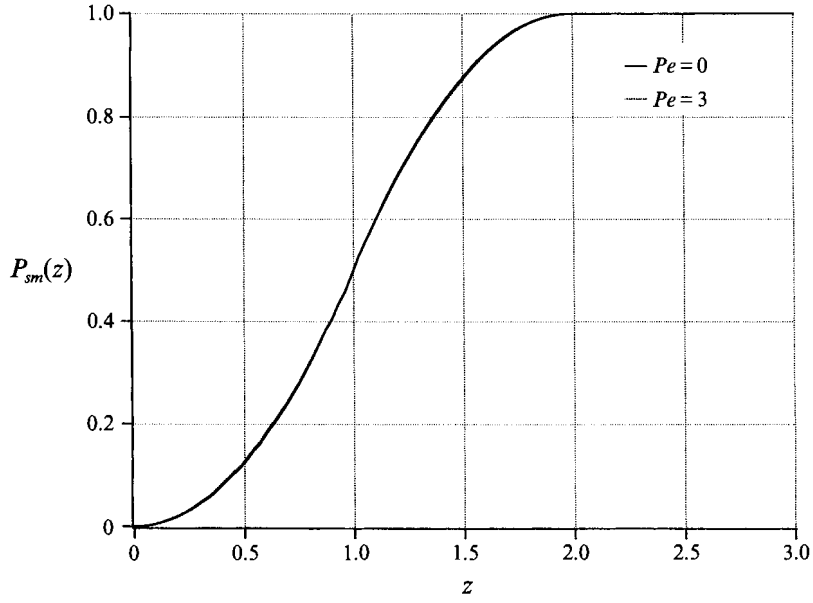

FIGURE 6. The segmental probability density function, $P_{sm}(z)$ at various shear rates: $Pe = 0$ and $Pe = 3$.

plus and minus one unit length away can intersect the point of interest. Near a boundary, z_1 and z_2 are constrained to lie within the natural domain of $z \in [0, \lambda]$. The functions $\theta_3(z_{eff})$ and $\theta_4(z_{eff})$ define the minimum and maximum angles in θ that a fibre with centre of mass at z_{eff} can have and still intersect the plane of interest, z. Carrying out this calculation, one can predict the segmental probability density function as depicted in figure 6. Like the centre-of-mass probability density function, the segmental probability density function is a weak function of Pe changing under flow at $O(Pe^2)$. This rather surprising result occurs because depletion of fibres at one orientation angle is balanced by accumulation of fibres at a symmetric angle relative to $\theta = \pi/2$. Accumulation of fibres at an orientation of $\theta = \pi/4$ balances depletion of fibres at an orientation of $\theta = 3\pi/4$. This occurs because the probability density function is antisymmetric in θ about $\pi/2$ at all powers in Pe considered here.

Once the flow is initiated, the fibres take a non-uniform distribution of orientations. Far from the walls, the fibres' most probable orientation is $\theta \approx \pi/4$ and $\phi \approx \pi/2$ and by symmetry $\theta \approx 3\pi/4$ and $\phi \approx 3\pi/2$. Under conditions of weak shear, Brownian motion tends to randomize the fibres' orientation distribution. However, the weak shear introduces an extensional component to the flow with the primary axis of extension at $\theta = \pi/4$. Thus, the fibres' most probable orientation is near this value (Bird & Warner 1971; Stewart & Sorensen 1972). As the shear rate increases, the most probable orientation angle increases until $\theta \approx \pi/2$ for high shear rates. Under conditions of strong Brownian motion, higher-order corrections in Pe to the orientation distribution function move the most probable orientation slightly off the primary axis of extension (Bird & Warner 1971; Stewart & Sorensen 1972). By solving the governing equations for the fibres' orientation distribution under conditions of strong shear and weak Brownian motion, Leal & Hinch (1971) showed that a fibre's most probable orientation is $\theta \approx \pi/2$. For the problem we consider where fibres experience weak shear and strong Brownian motion, it is physically

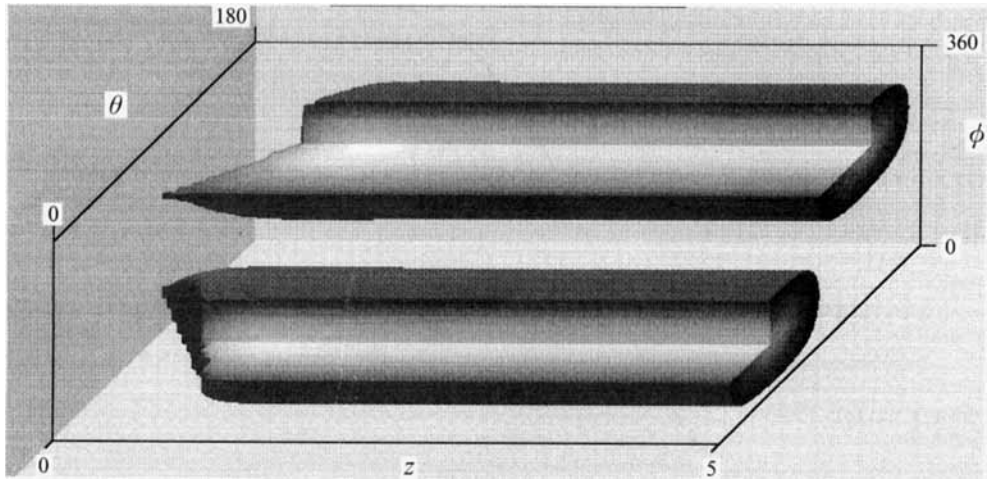

FIGURE 7. The fibre probability density function, $P(z, \theta, \phi)$, for a shear flow where $Pe = 1$ and a gap width $\lambda = 10$. Since the probability density function under shear flow is symmetric about the centre of the gap, the function is only plotted for half of the entire channel where $z \leqslant 5$.

correct to expect the probability density function to reach a maximum when the fibres are aligned with the primary axis of the extensional part of the flow.

Near a wall, the set of allowed fibre orientations, i.e. the available θ-orientation, is reduced from that in the bulk. At the wall the only allowed θ-orientation is $\theta = \pi/2$. In figure 7 the probability density function described by equation (5.4) for rigid fibres under shear flow is plotted. This plot has been constructed such that the three independent variables (z, θ and ϕ) span the three orthogonal faces of a cube. At each point within this cube the value of the probability density corresponding to the value of z, θ and ϕ at that point is marked via a shading scheme. High probability values are bright while low probability values are dark. In order to see the important structure of the probability density function, regions of very low probability have been made transparent in figure 7 and slices have been removed from regions of high probability to show their internal structure. Figure 7 shows the probability density function over half of the gap, $z \in [0, \lambda/2]$, for a total gap width of $\lambda = 10$ at $Pe = 1$ and a fibre concentration of $c = 1$. Since the shear flow probability density function is symmetric about the centreline of the channel, a mirror image of figure 7 exists for $z \in [\lambda/2, \lambda]$. Examination of this probability density function shows that far from the walls in the centre of the channel, hydrodynamic forces cause the fibre's most probable orientation to lie near the primary axis of extension, $\theta \approx \pi/4$, $\phi \approx \pi/2$ and $\theta \approx 3\pi/4$, $\phi \approx 3\pi/2$ as mentioned previously. Approaching a wall, the hydrodynamic alignment of the fibres is reduced and the tendency to line up with the primary axis of extension is weakened since the wall dominates the fibre's environment. Near these boundaries, the allowed configurations in θ decrease leaving a wedge shaped region of allowed configurations. As shown in figure 7, the probability density function is changing rapidly over the length of a fibre as it approaches a wall. Thus, fibres near a wall are experiencing a concentration field that changes rapidly along their length. Also, since Brownian forces and torques are proportional to gradients of the probability density function, the Brownian forces and torques felt by a fibre are changing rapidly within this depletion region. The rapidly changing concentration field and Brownian forces supports the initial assertion that to understand these wall

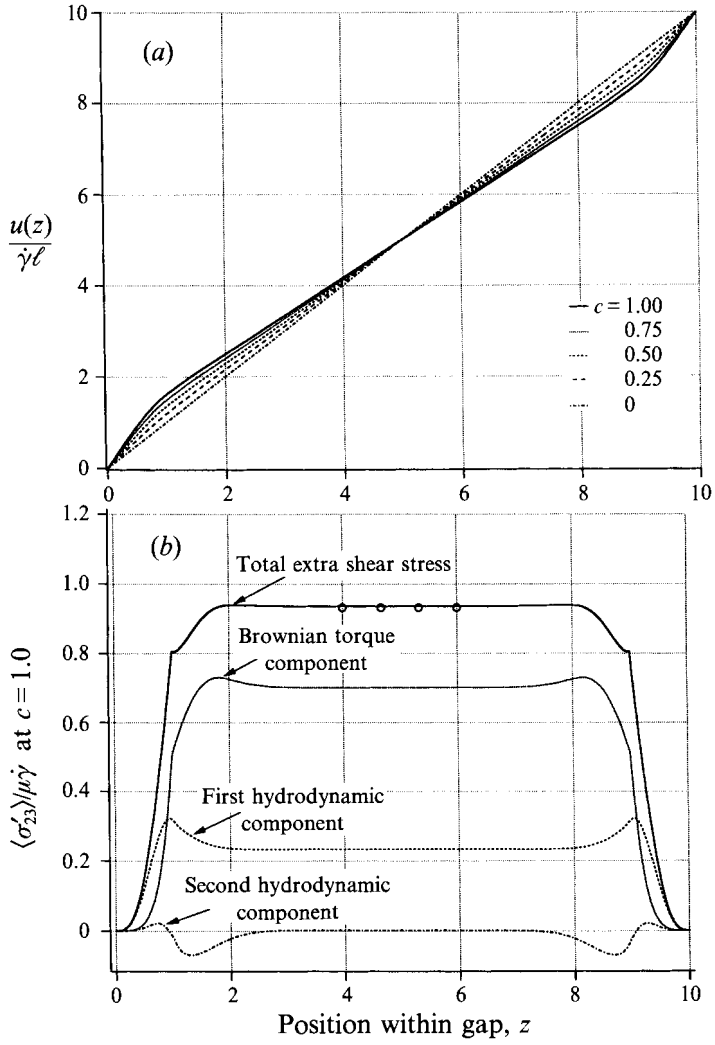

FIGURE 8. (*a*) Velocity profiles for a gap width of $\lambda = 10.0$ and fibre concentrations of $0 \leqslant c \leqslant 1.0$. (*b*) Extra shear stress profiles for $\lambda = 10.0$ and $c = 1.0$. Open circles denote the extra shear stress predicted by Hinch & Leal (1972) evaluated at a fibre concentration of $c = 1.0$ and at the local shear rate.

regimes one must consider the fibres in a nonlocal environment. Not surprisingly, the average velocity field also changes rapidly near the flow boundaries as shown below.

Plotted in figures 8, 9 and 10 are velocity and extra shear stress profiles as a function of position within the gap for gap widths of $\lambda = 10, 4$ and 1 respectively. In figure 8 it is evident that the velocity distribution is stratified into three distinct regions. In the core of the channel, the profile is flat with shear rate slightly below the bulk applied shear rate for all $c > 0$. Near the walls are the two other flow regions in which the velocity changes rapidly to match the no-slip condition at either wall. Comparing the velocity profile to the corresponding extra stress profile in figure 8 one can see the total extra stress is constant in the core of the channel. Near the walls, the extra stress rapidly drops to zero. Within the core of the channel, the extra stress is dominated by its Brownian component. However, approaching the wall, the Brownian

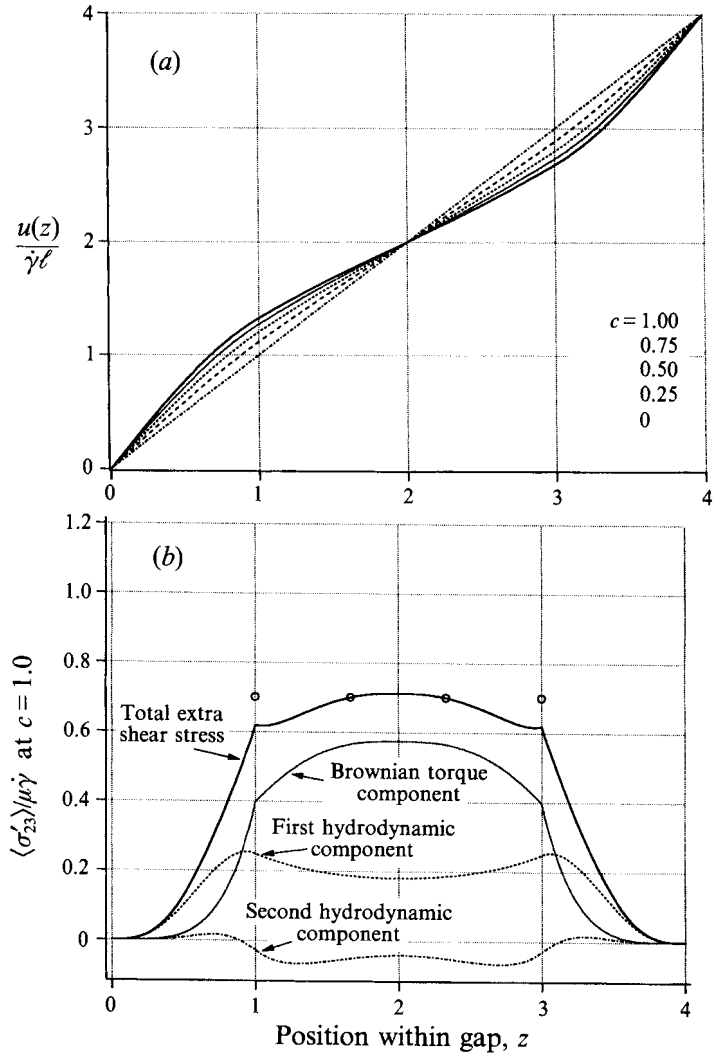

FIGURE 9. As figure 8 but for a gap width of $\lambda = 4.0$.

component decays sooner than either of the two hydrodynamic components. The smaller hydrodynamic component is the extra stress associated with the inability of a rigid fibre to rotate with the perpendicular component of the fluid velocity when that velocity varies along the fibre's length. Only near the walls where the fluid velocity is changing rapidly on the length of a fibre does this component of the stress become non-zero. Open circles in the extra stress plot correspond to unbound suspension properties predicted elsewhere (Giesekus 1962; Hinch & Leal 1972) and evaluated at the local shear rate at the channel's centre. By comparison with the bulk theoretical predictions, one sees that the core of the solution behaves as if it were unbound. The walls strongly affect the region within one full rod length 2ℓ, but diminish quickly thereafter.

To allow easy comparison of the data in figures 8, 9 and 10, the extra shear stresses have been normalized for equilibrium with an unbound suspension. As mentioned earlier, this normalization is equivalent to replacing the normalization

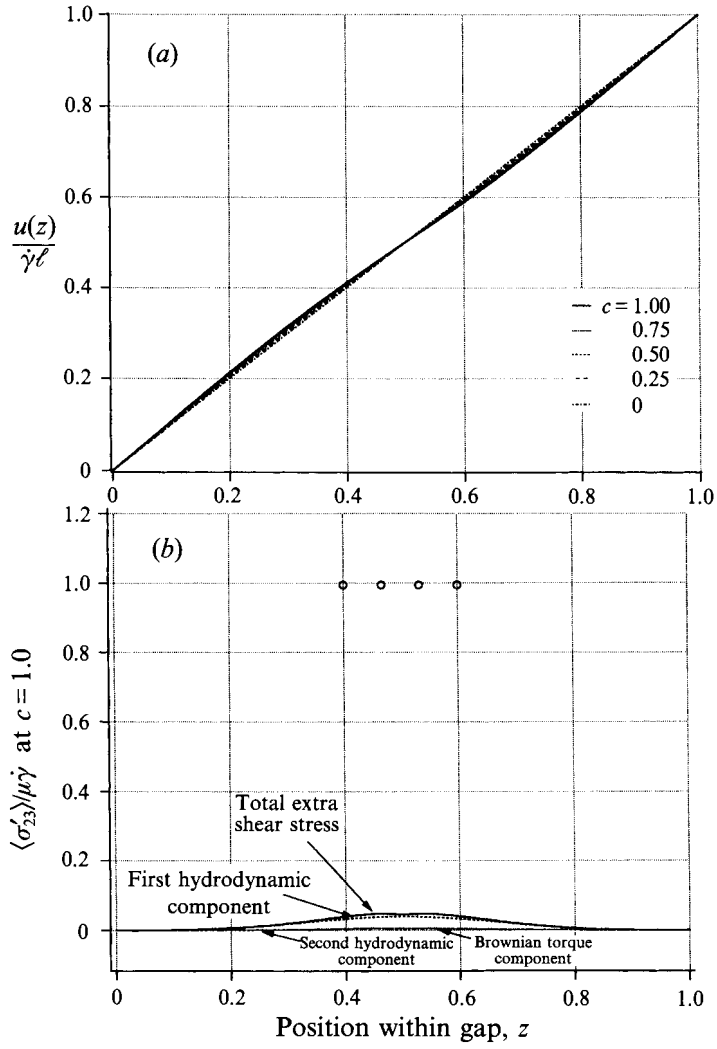

FIGURE 10. As figure 8 but for a gap width of $\lambda = 1.0$.

function $M(\lambda)$ by the factor $1/(4\pi)$. Physically this corresponds to making the fluid between the parallel plates in equilibrium with an unbound suspension of fibres at the same concentration. Using this normalization, a concentration, c_O, at one gap width is directly comparable to the same concentration at a different gap. Without this normalization, the concentration of the suspension between the parallel plates would fractionally change as the gap size changes as described earlier in §3. For the detailed calculations of the velocity profile, extra stresses and probability density, this normalization is immaterial. However to aid understanding, it is easiest to present our results assuming the confined suspension is in equilibrium with an unbound suspension of a given concentration.

In figure 9 are plotted velocity and extra stress profiles at a gap width of $\lambda = 4$, for the same; concentrations and shear rates as in figure 8 where the gap width was $\lambda = 10$. Note that the size of the slip region has remained the same; however the magnitude of the slip is larger than in figure 8 relative to the upper plate velocity. The

velocity profile is strongly nonlinear in figure 9 because the depletion layers at either wall are within a full fibre length of each other and can thus interact. As before, the extra stress profile shown in figure 9 is a maximum at the centre of the channel where the Brownian component dominates. However, the solution at the centre no longer behaves like an unbound suspension as demonstrated by the reduction in stress relative to the extra shear stress for an unbound suspension of slender Brownian rods evaluated at the centreline shear rate, cf. figure 9. Approaching either wall, the Brownian extra stress decays followed by the hydrodynamic stresses and both vanish identically at the bounding surfaces.

At still smaller gaps, the velocity and stress profiles are plotted in figure 10 where $\lambda = 1$. The velocity profile is almost linear as was found for much larger gaps. The slip regions encountered earlier are essentially absent. This occurs because the extremely narrow gap confines the slender fibres to orientations nearly parallel with the walls, $\theta \approx \pi/2$. In these orientations, the large aspect ratio fibres have a minimal effect on the stress and hence the flow. Note also that in contrast to our previous calculations, the hydrodynamic extra shear stress dominates over the Brownian extra shear stress throughout the entire channel.

6.1. *Asymptotic results for small fibre concentration and small gap*

Since the velocity profile is linear for small gap widths (as demonstrated by our numerical calculations) and it is linear as well in the limit of small fibre concentrations, simple analytic expressions can be calculated for the probability density and, therefore, the extra stress in these two distinguished limits. Although different asymptotes, there are a number of similarities in the analysis of these limits. Thus we shall develop an asymptotic solution as $c \to 0$ (finite λ) first, and then return to a brief discussion of the related limit $\lambda \to 0$ (finite c).

For linear velocity profiles, the probability density ceases to depend on position within the gap, except for the excluded angles due to the bounding surfaces. In the limit of zero fibre concentration, $P(z, \theta, \phi)$ will be small throughout the gap. Thus, ignoring changes in the probability density function near the walls will induce an error of $O(c|\lambda - 2\ell|)$ when one assumes $P(z, \theta, \phi) \to n\Phi(\theta, \phi)$ where $\theta \in [\theta_1(z), \theta_2(z)]$ as $c \to 0$. It follows that the only z-dependence of the probability density function occurs in the definition of the allowed set of orientation angles $\theta_1(z)$ and $\theta_2(z)$. With these approximations, the orientation distribution function $\Phi(\theta, \phi)$ in the small concentration limit can be derived from equation (3.6) or equivalently, following the work of Bird & Warner (1971) and Stewart & Sorensen (1972). To first order in Péclet number, the fibre orientation distribution becomes

$$\lim_{c\to 0} P(z, \theta, \phi) \text{ or } \lim_{\lambda\to 0} P(z, \theta, \phi) = n\Phi(\theta, \phi) \approx nM(\lambda)\left\{1 + Pe\tfrac{1}{2} \sin\phi \sin\theta \cos\theta\right\}. \tag{6.3}$$

Using this orientation distribution function confined to the reduced set of orientation angles, $\theta_1(z)$ and $\theta_2(z)$ defined in equations (3.16) and (3.17), calculation of the extra shear stress from equations (2.19)–(2.21), (2.24) and (2.25) is straightforward. The extra shear stress becomes

$$\langle \sigma'_{23} \rangle = \tfrac{4}{3}\pi^2 M(\lambda)\, \mu\dot{\gamma} c S(z) \tag{6.4}$$

where $S(z)$ is defined as

$$S(z) = \begin{cases} \frac{2}{15}(5z^3 - 3z^5) + \frac{21}{40}z^5 & \text{for } 0 \leqslant z \leqslant 1 \\ \frac{4}{15} + \frac{1}{40}(40z^2 - 20z^3 + z^5) & \text{for } 1 \leqslant z \leqslant 2 \\ \frac{4}{15} + \frac{4}{5} & \text{for } 2 \leqslant z \leqslant (\lambda/2). \end{cases} \tag{6.5}$$

The function $S(z)$ is a geometric function defining the shape of the stress profile while the prefactor to $S(z)$ in equation (6.4) governs the magnitude of the stress. The first terms in $S(z)$ arise from the first hydrodynamic component of the extra stress while the second term derives from the Brownian component. Thus, the hydrodynamic stresses scale as z^3 for $z < 1$ while the Brownian contribution to the shear stress scales as z^5. It is expected therefore that for small gap widths, i.e. $\lambda \leqslant 2$, the hydrodynamic contribution to the shear stress should dominate the Brownian contribution as was evident in figure 10. Note finally that, since the shear stress is symmetric about the centreline of the channel, $z = \lambda/2$, only the shear stress for the lower half of the channel is presented in equations (6.4) and (6.5).

Since the total shear stress is constant on any plane parallel to the walls, one can use equation (6.4) to calculate the local shear rate as a function of position within the gap. Adding the fluid contribution to the extra stress in equation (6.4), the total shear stress is

$$\langle \sigma_{23} \rangle = \dot{\gamma}(z) + \tfrac{4}{3}\pi^2 M(\lambda) c\, \dot{\gamma}(z)\, S(z), \tag{6.6}$$

where the shear stress has been made dimensionless with the applied shear rate, $\overline{U}/(\lambda \ell)$, times the solvent viscosity, μ. From equation (6.6), the shear rate as a function of position within the gap becomes

$$\dot{\gamma}(z) = \frac{1}{1 + \frac{4}{3}\pi^2 M(\lambda)\, c\, S(z)}. \tag{6.7}$$

Given the shear stress and shear rate from equations (6.4) and (6.7), the velocity profile in the limit of zero fibre concentration becomes

$$u(z) = z + \frac{z}{\lambda}\int_0^{\lambda} \tfrac{4}{3}\pi^2 M(\lambda)\, c\, \dot{\gamma}(\xi)\, S(\xi)\, \mathrm{d}\xi - \int_0^{z} \tfrac{4}{3}\pi^2 M(\lambda)\, c\, \dot{\gamma}(\xi)\, S(\xi)\, \mathrm{d}\xi. \tag{6.8}$$

Figure 11 compares the asymptotically calculated velocity and stress profiles at a concentration of $c = 0.5$ to the actual profiles calculated via the full numerical solution of the governing equations. The asymptotic solutions recover all the qualitative features of the extra shear stress and the velocity profiles found in the fully self-consistent calculations.

Since the only assumption made in deriving the results (6.3)–(6.8) was that the velocity profile was approximately linear, it follows that all these results are similarly valid in the limit of small gap, i.e. $\lambda \to 0$, $c \sim O(1)$. Of course, we must expand each equation for $\lambda \ll 1$. Thus the shape function, $S(z)$, becomes

$$S(z) = \tfrac{2}{3}z^3. \tag{6.9}$$

With an asymptotic theory for both small concentration and small gap width, simple predictions can be made about the suspension's effective properties. In the following subsection we will compare the effective rheology predicted via the fully self-consistent theory with this simple asymptotic theory.

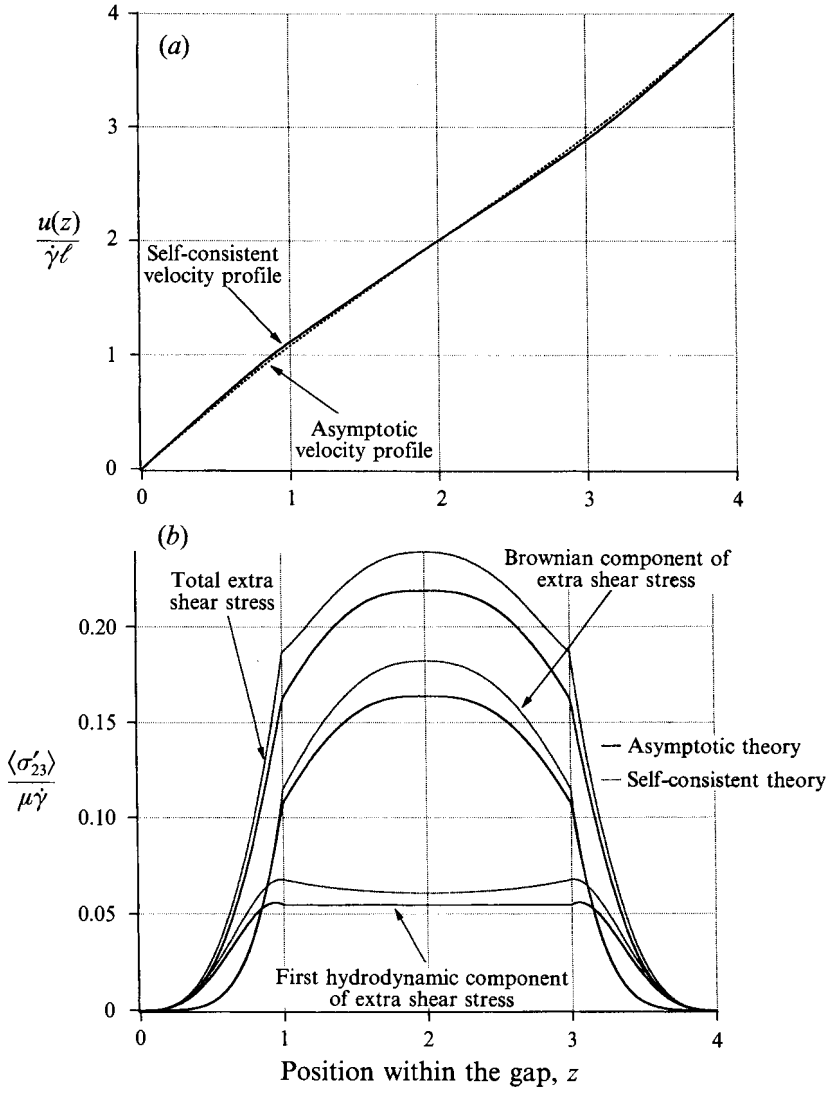

FIGURE 11. (*a*) Velocity and (*b*) extra shear stress profiles for a gap width of $\lambda = 4$ and a fibre concentration of $c = 0.25$ as predicted by the the self-consistent, nonlocal theory and the dilute asymptotic theory.

6.2. *Effective rheology*

To examine the effects of the confining walls on the effective rheology of the thin layer, we first define

$$\overline{\mu}_{eff}(z) = \mu + \frac{\langle\sigma'_{23}\rangle(z)}{\dot{\gamma}} \tag{6.10}$$

as the effective viscosity of the suspension at a given point, z, within the gap and

$$\mu_{eff} = \frac{1}{\lambda}\int_0^{\lambda} \overline{\mu}_{eff}(z)\mathrm{d}z \tag{6.11}$$

as the average effective viscosity of the suspension for a fixed gap width, λ. Note that μ_{eff} also equals the ratio of the shear stress to the shear rate at the moving plate in our parallel plate geometry. In the absence of confining walls, μ_{eff} equals the effective viscosity of an unbound suspension since, in this instance, the centre of mass and orientational distribution of fibres would be uniform. Thus, if the suspension were locally homogeneous, then neither the shear rate nor shear stress would depend on z and it follows that

$$\lim_{\lambda\to\infty}\mu_{eff} = \lim_{\lambda\to\infty}\frac{1}{\lambda}\int_0^\lambda \frac{\langle\sigma_{23}\rangle}{\dot\gamma}\mathrm{d}z = \frac{\langle\sigma_{23}\rangle_{unb}}{\dot\gamma_{unb}}\lim_{\lambda\to\infty}\frac{1}{\lambda}\int_0^\lambda \mathrm{d}z = \mu_{unb} \tag{6.12}$$

where the terms subscripted with *unb* refer to shear stress and shear rate in an unbound suspension. Therefore, the effective viscosity averaged over the entire gap approaches the effective viscosity of an unbound suspension as the gap becomes infinitely large.

Using the asymptotic formula for the extra stress defined in equation (6.4), and the asymptotic shear rate defined in equation (6.7), the average effective viscosity to first order in concentration can be found as

$$\frac{\mu_{eff}}{\mu} = 1 + \tfrac{4}{3}\pi^2 M(\lambda)c\begin{cases}\dfrac{\lambda^3\left(32+\lambda^2\right)}{1536} & \text{for } 0\leqslant\lambda\leqslant 2\\[2ex] \dfrac{\lambda^6-120\lambda^4+640\lambda^3+2048\lambda-4480}{7680\lambda} & \text{for } 2\leqslant\lambda\leqslant 4\\[2ex] \dfrac{64\lambda-115}{60\lambda} & \text{for } \lambda\geqslant 4.\end{cases} \tag{6.13}$$

The limiting behaviour for the effective viscosity in the small gap limit (for $c\sim O(1)$) found from expanding 6.13 for $\lambda \ll 1$ is

$$\lim_{\lambda\to 0}\frac{\mu_{eff}}{\mu} = 1 + \frac{4}{3}\pi^2 M(\lambda)\, c\,\frac{\lambda^3}{48}. \tag{6.14}$$

In figure 12 the zero shear rate, effective viscosity as defined by (6.11) is plotted as a function of gap width and concentration. The dashed lines represent the asymptotic small concentration approximation defined above and also included are the predictions for an unbound suspension by Hinch & Leal (1972). The three different graphs in this figure represent three different ways of understanding the data and help explain the basic scaling behind the effective viscosity.

Figure 12(*a*) represents the average effective viscosity normalized for a reduced available volume discussed in §3; it is the averaged effective viscosity for a suspension confined between two infinite, parallel plates. Figure 12(*b*) represents the average effective viscosity for a suspension normalized to be in equilibrium with an unbound suspension of fibres at the same number density n. Thus, the effective viscosity in figure 12(*b*) corresponds to that which is more easily measurable in an actual experiment where a confined fluid under flow is in equilibrium with an unbound suspension.

For both normalizations of the effective viscosity, in figures 12(*a*) and 12(*b*), there is a strong dependence of effective viscosity on gap especially for higher concentrations. Very large gaps ($\lambda > 30$) are required before the total solution effective viscosity approaches the predicted effective viscosity for an unbound suspension predicted by Hinch & Leal (1972).

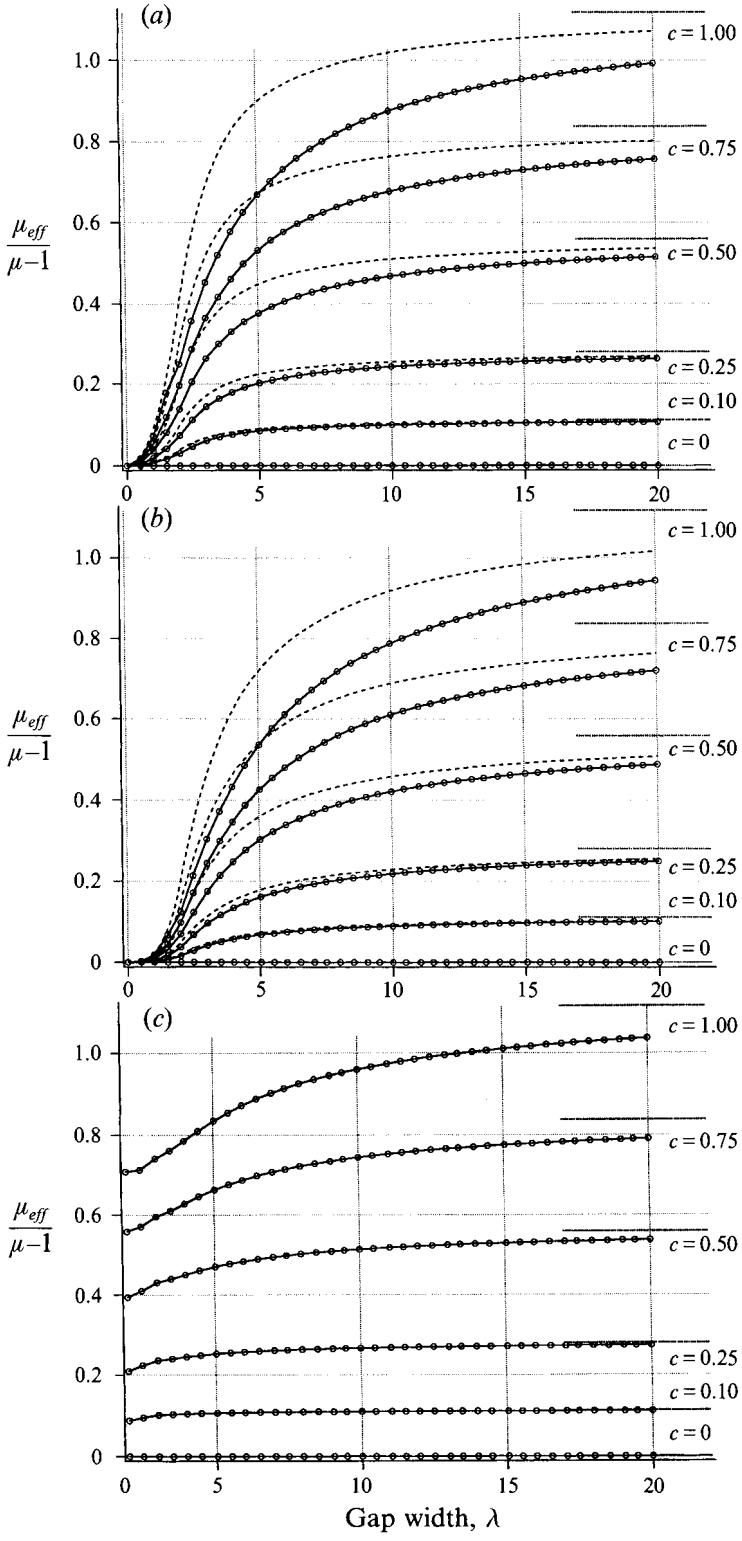

FIGURE 12. For caption see facing page

The asymptotic solution, in the limit $c \to 0$ ($\lambda \sim O(1)$), for the effective viscosity derived in equation (6.13) shows a scaling of the effective viscosity with total gap width. The primary assumptions made in the derivation of equation (6.13) were that the concentration was vanishingly small, $c \to 0$ and that the rigorous no-flux constraints on the probability density function, equations (3.12) and (3.13), could be ignored provided the reduction in available fibre orientations near a wall, equations (3.16) and (3.17), is enforced. If the scaling of the effective viscosity in equation (6.13) is valid for all concentrations then dividing the effective viscosity data in figure 12(*b*) by the gap width scaling of equation (6.13) should reduce the data to a set of straight lines. Plotted in figure 12(*c*) is the average effective viscosity data from figure 12(*b*) with the gap width scaling of equation (6.13) factored out. As is evident from figure 12(*c*), this scaling does an excellent job at low concentration and medium gap widths in explaining the reduced effective viscosity found in bound suspensions. At larger concentrations, this asymptotic theory does not fully account for the reduction in effective viscosity.

In the previous discussion of velocity profiles for various gap widths and concentrations, reference was made to the non-monotonic behaviour of the apparent slip velocity as a function of gap width. Figure 13(*a*) shows the slip velocity (where slip velocity is defined as the expected velocity at the wall if the velocity is linearly extrapolated from the velocity profile at the centre of the channel) scaled by the upper plate velocity for various gap widths and concentrations. One can see that the magnitude of the slip relative to the upper plate velocity is a maximum for gaps near $\lambda = 4$ for all concentrations. Plotted in figure 13(*b*) is the expected slip velocity as a function of gap width and concentration made dimensionless with $\dot{\gamma}\ell$ which is a characteristic velocity difference over a distance ℓ, the scale of the velocity slip. Examination of this slip velocity plot, figure 13(*b*), shows that as the gap width grows, a constant, concentration-dependent slip layer develops and remains for all larger gaps. Additionally, the slip expected for infinitely large gaps, made dimensionless with $\dot{\gamma}\ell$ as a function of concentration is plotted in figure 14. For the concentrations investigated in this work, the slip velocity under shear flow grows approximately linearly with fibre concentration at large gaps.

6.3. *Normal stresses*

Apart from the extra particle shear stresses, normal stress differences occur in Brownian fibre suspensions and can be predicted by our nonlocal theory. In figure 15, the first and second normal stress differences are plotted for a concentration of $c = 1.0$ and gap widths of $\lambda = 10, 4$ and 1 as a function of position within the gap, z. The first normal stress difference is defined in the usual fashion as $N_1 = \langle\sigma_{22}\rangle - \langle\sigma_{33}\rangle$ and the second normal stress difference as $N_2 = \langle\sigma_{33}\rangle - \langle\sigma_{11}\rangle$. Notice that both normal stresses go through a region of overshoot near the walls where the normal stress difference is greater than it is in the core. By studying normal stress

FIGURE 12. Effective viscosity of a confined suspension under shear as a function of gap width and fibre concentration. In all three figures the open circles connected with lines represent the self-consistent, nonlocal theory, while the large-dashed lines represent the asymptotic theory and the small-dashed lines represent the predictions of Hinch & Leal (1972) for the effective viscosity of an unbound fibre suspension at the concentration indicated. In (*a*) the data are normalized for a reduced available volume, while in (*b*) and (*c*) the data are normalized to be in equilibrium with an unbound suspension at the same concentration as described in the text.

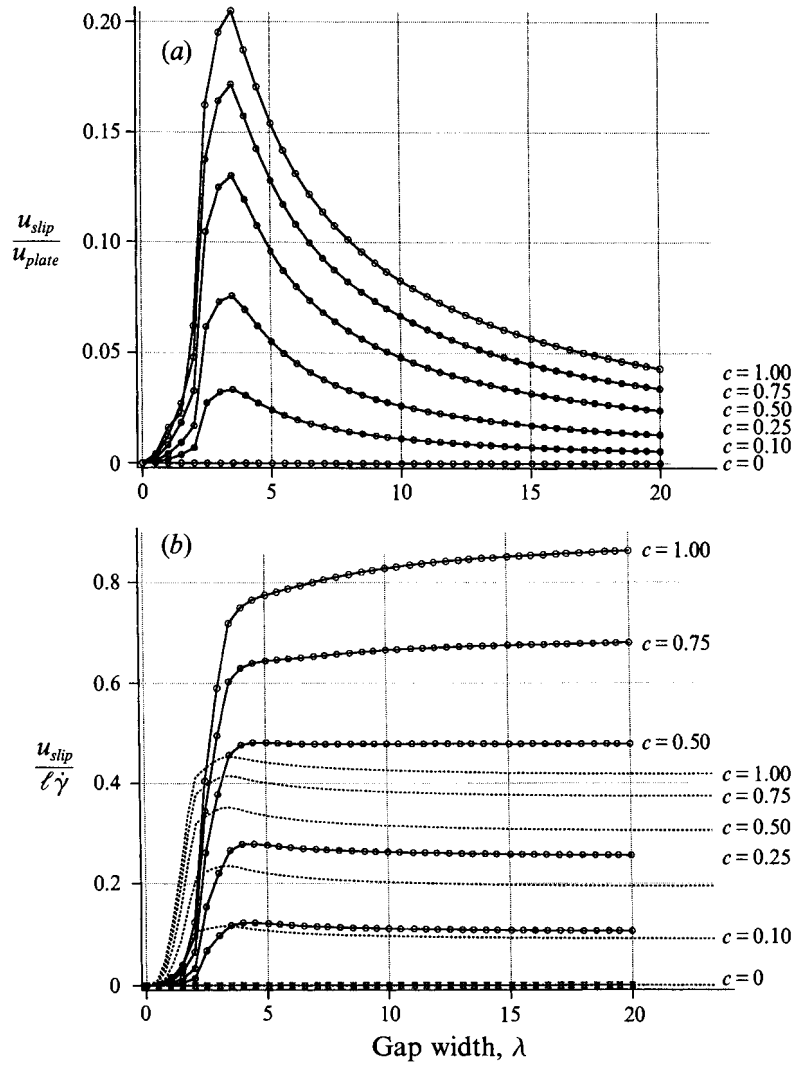

FIGURE 13. Slip velocity for a confined fibre suspension as a function of gap width and concentration. In (*a*) the slip velocity is made dimensionless with the upper plate velocity, u_{plate} while in (*b*) the slip velocity is made dimensionless with the characteristic velocity $\dot{\gamma}\ell$. Open circles connected with lines represent the self-consistent, nonlocal theory, while the large-dashed lines represent the asymptotic theory.

profiles at several concentrations, this non-monotonic behaviour near the wall was determined to be a concentration effect. That is, as the fibre concentration goes to zero, the overshoots near the wall vanish. In the limit of $c \to 0$ the first normal stress difference decays monotonically from its core value to zero at the wall while the second normal stress difference goes from its negative value in the channel's centre to a positive value near the wall, and finally to zero at the bounding surface.

For all gap widths and concentrations, the second normal stress difference is positive for short distances from the wall. In very narrow gaps, the second normal

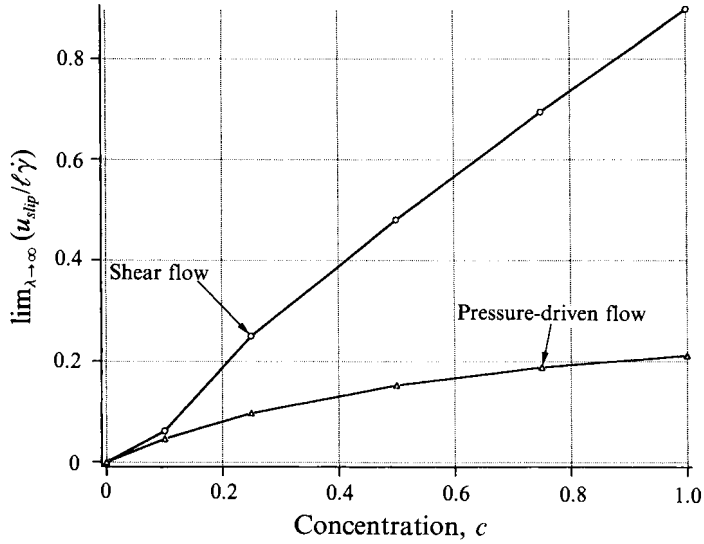

FIGURE 14. Slip velocity for a confined fibre suspension in the limit of infinite gap width as a function of fibre concentration for suspensions under shear and pressure-driven flow.

stress difference is always positive as shown in figure 15(*c*). Near a wall in both large and small gaps, the second normal stress difference becomes positive for the same reason. A rigid fibre rotating in a Jeffery's orbit will rotate in both the θ- and ϕ-directions. When a fibre is near a boundary under the shear flow shown in figure 3, rotation in the θ-direction will be hindered while rotation in the ϕ-direction will not. While the hydrodynamic forces from the shear flow tend to align the fibres with the flow where $\phi \approx \pi/2$, the larger magnitude Brownian forces tend to randomize a fibre's orientation. Rotation in the ϕ-direction near a wall in the (x_1, x_2) plane from Brownian torques results in the positive second normal stress difference.

In figure 16 the normal stress differences at the centre of the channel are plotted as a function of the gap width using concentration as a parameter. Dashed lines represent predictions by Hinch & Leal (1972) for normal stress differences in unbound fibre suspensions. For small gaps, both the first and second normal stress differences are positive. Once the gap width becomes larger than the full rod length, the second normal stress becomes negative and begins approaching its expected bulk value. The first normal stress difference remains positive for all gap widths and approaches the expected value for unbound suspensions quickly for low concentrations but much more slowly at high concentrations.

7. Pressure-driven flow

Holding the upper plate fixed and applying a pressure gradient in the x_2-direction in figure 3 results in pressure-driven flow within the channel. For this flow, the same governing equations are solved as in the shear flow case, but with a zero fluid velocity boundary condition at each wall.

For large gaps, the pressure-driven flow near the wall is equivalent to a simple shear flow. As such, the probability density function for pressure-driven flow in a large gap ($\lambda = 10$) is similar to that for a shear flow near the wall.

In figure 17 regions of high probability in fibre configuration space are plotted

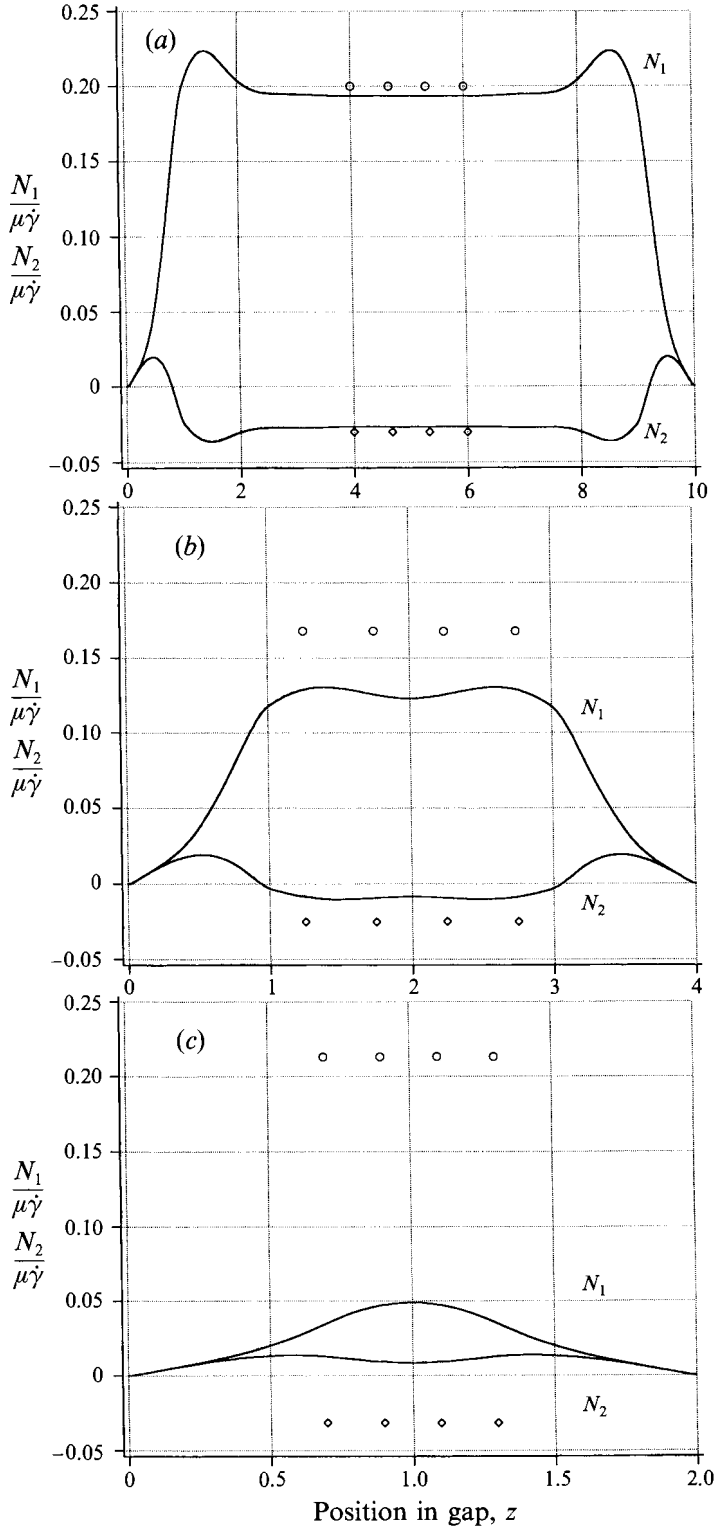

FIGURE 15. For caption see facing page

for fibres in planar pressure-driven flow at a concentration of $c = 1$, a gap width of $\lambda = 10$ and $Pe = 1$ as was done earlier for shear flow, cf. figure 7. For this figure, the probability density function is only plotted for half the channel, being antisymmetric about the channel centreline. Near each wall, the probability density function is changing rapidly on the length scale of a fibre. At the centre of the channel, where the local shear rate is zero, there is little preference for any orientation as Brownian motion fully randomizes the fibres' orientation.

For moderate and small gaps, the probability density function changes on the length scale of a fibre across the entire gap. Plotted in figure 18 is the probability density function for a gap of two full fibre lengths, $\lambda = 4$, at the same concentration and wall shear rate as before, $c = 1$ and $Pe = 1$ respectively. For these small gaps, the local curvature in the velocity field occurs on lengths smaller than a fibre length. Thus the probability density function is affected by the curvature of the velocity field, not just the local effective shear rate. Again it is evident that the probability density function is changing rapidly, and the problem is nonlocal.

Shown in figures 19, 20 and 21 are velocity and extra shear stress profiles for gap widths of $\lambda = 10, 4$ and 1 respectively. As was the case with shear flow, the large gap pressure-driven velocity profiles have three distinct regions. In the centre of the channel is the core flow where the field is strongly effected by the presence of the rods. The core velocity profile is flattened or thickened due to the extra stress associated with the rods. Approaching either wall one sees the depletion region where the extra shear stress goes to zero and the local shear rate increases rapidly as the fluid thins. The extra shear stress profiles show that the extra stress components all vary linearly in the centre of the channel with local shear rate. However as a boundary is approached, all three components rapidly diminish. As before the Brownian component decays at a full fibre length followed by the two hydrodynamic components.

At the intermediate gap width of $\lambda = 4$, shown in figure 20, the flattening of the velocity profile is stronger than at larger gaps widths, but the regions near the wall are unchanged. Examination of the extra shear stress as a function of position within the gap shows the same trend as before where the Brownian component decays before the hydrodynamic components.

Finally, for very narrow gaps, the velocity field remains almost unchanged for various fibre concentrations as shown in figure 21 where $\lambda = 1$. As was the case with shear flow, the extra shear stress due to the fibres is much weaker for narrow gaps, and the hydrodynamic extra shear stresses dominate over their Brownian counterparts across the entire gap.

7.1. *Asymptotic solution for small fibre concentration and small gap*

As was done for shear flow in the previous section, asymptotic solutions for the probability density, extra shear stress and velocity can be determined in the limit of zero fibre concentration and separately in the limit of small gap width. To first order

FIGURE 15. First and second normal stress differences for a confined suspension of slender fibres as a function of position within the gap for a fibre concentration of $c = 1.0$: (*a*) represents a total gap width of $\lambda = 10$, (*b*) a gap width of $\lambda = 4$ and (*c*) a total gap width of $\lambda = 2.0$ Open circles denote the normal stress differences predicted by Hinch & Leal (1972) evaluated at a fibre concentration of $c = 1.0$ and at the local shear rate.

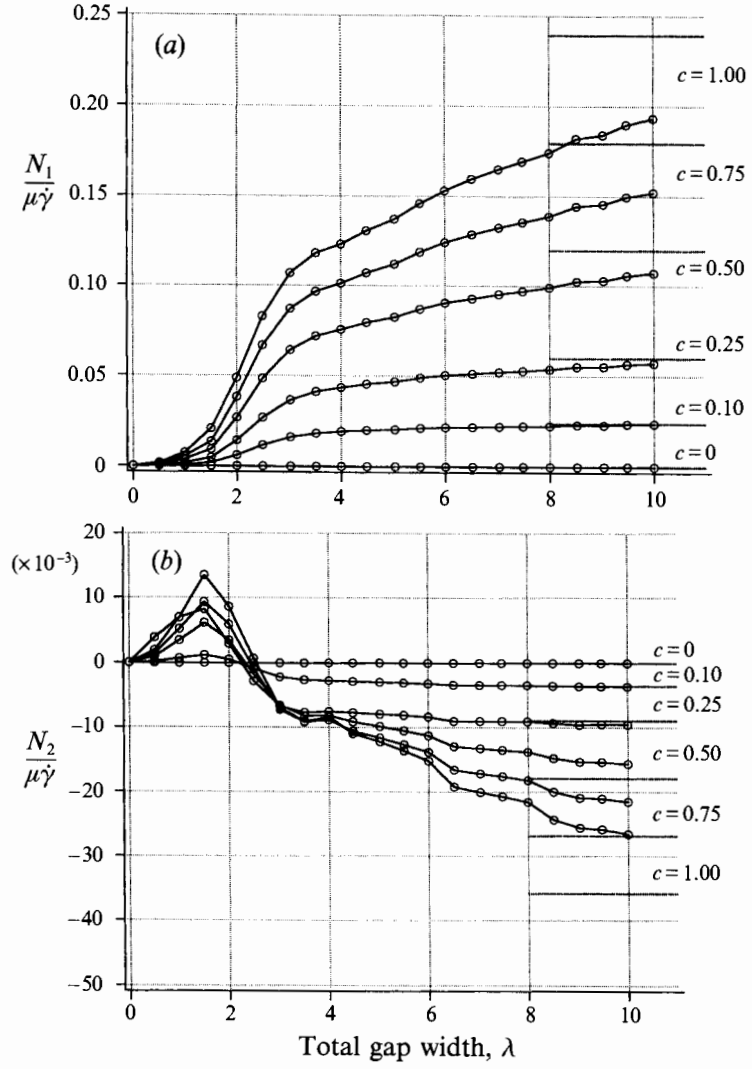

FIGURE 16. (*a*) First and (*b*) second normal stress differences at the centre of the channel as a function of total gap width and fibre concentration. Open circles connected by lines represent the predictions of the self-consistent nonlocal theory, while dashed lines represent the normal stress differences predicted by Hinch & Leal (1972) evaluated at the indicated fibre concentration and at the shear rate applied across the entire gap.

in Péclet number the fibre orientation distribution becomes

$$\lim_{c\to 0} P(z,\theta,\phi) \text{ or } \lim_{\lambda\to 0} P(z,\theta,\phi) = n\Phi(\theta,\phi)$$
$$\approx nM(\lambda)\left\{1 + Pe\frac{1}{2}\left(1 - \frac{2z}{\lambda}\right)\sin\phi\,\sin\theta\,\cos\theta\right\}. \tag{7.1}$$

Using this orientation distribution function confined to the reduced set of orientation angles, $\theta_1(z)$ and $\theta_2(z)$, calculation of the extra shear stress from equations (2.19)–

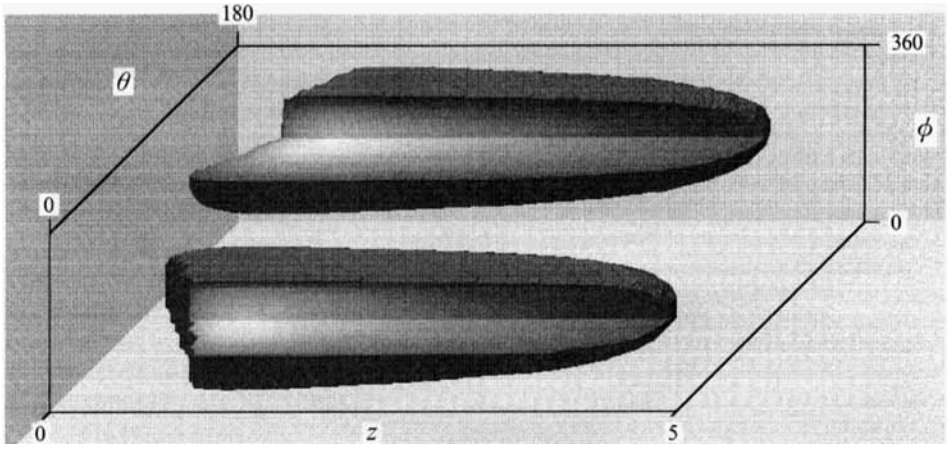

FIGURE 17. The fibre probability density function, $P(z,\theta,\phi)$, for pressure-driven flow where $Pe = 1$ and the gap width is $\lambda = 10$. Since the probability density function under pressure-driven flow is antisymmetric about the centre of the gap, the function is only plotted for half of the entire channel where $z \leqslant 5$.

(2.21), (2.24) and (2.25) results in

$$\langle \sigma'_{23} \rangle = \tfrac{4}{3}\pi^2 M(\lambda)\,\mu\dot{\gamma} c S(z) \tag{7.2}$$

with $S(z)$ is defined as

$$S(z) = \begin{cases} \dfrac{2}{15}(5z^3 - 3z^5) + \dfrac{7z^5}{160}\left(\dfrac{12\lambda - 29z}{\lambda - 2z}\right) & \text{for } 0 \leqslant z \leqslant 1 \\ \dfrac{4}{15} + \dfrac{z^2}{160}\left(\dfrac{-240 + 160\lambda - 80\lambda z + 40z^2 + 4\lambda z^3 - 3z^4}{\lambda - 2z}\right) & \text{for } 1 \leqslant z \leqslant 2 \\ \dfrac{4}{15} + \dfrac{4}{5} & \text{for } 2 \leqslant z \leqslant (\lambda/2). \end{cases} \tag{7.3}$$

Since the shear stress is odd about the centreline of the channel, $z = \lambda/2$, the shear stress for the upper half of the channel is the same as the shear stress show in equations (7.2) and (7.3) but with the opposite sign. As before, the hydrodynamic stresses scale as z^3 for $z < 1$ while the Brownian contribution to the shear stress scales as z^5.

The dimensionless local shear rate as a function of position within the gap can be calculated as before yielding

$$\dot{\gamma}(z) = \frac{(1 - 2z/\lambda)}{1 + \tfrac{4}{3}\pi^2 M(\lambda)\, c\, S(z)} \tag{7.4}$$

where we recall that the shear rate has been made dimensionless with the shear rate at the wall.

From the shear stress and shear rate expressions, equations (7.2) and (7.4), the velocity profile in the limit of zero fibre concentration is

$$u(z) = \frac{z}{\lambda}(\lambda - z) - \int_0^z \tfrac{4}{3}\pi^2 M(\lambda)\, c\, \dot{\gamma}(\xi)\, S(\xi)\, \mathrm{d}\xi. \tag{7.5}$$

A comparison between the asymptotically calculated velocity and stress profiles and

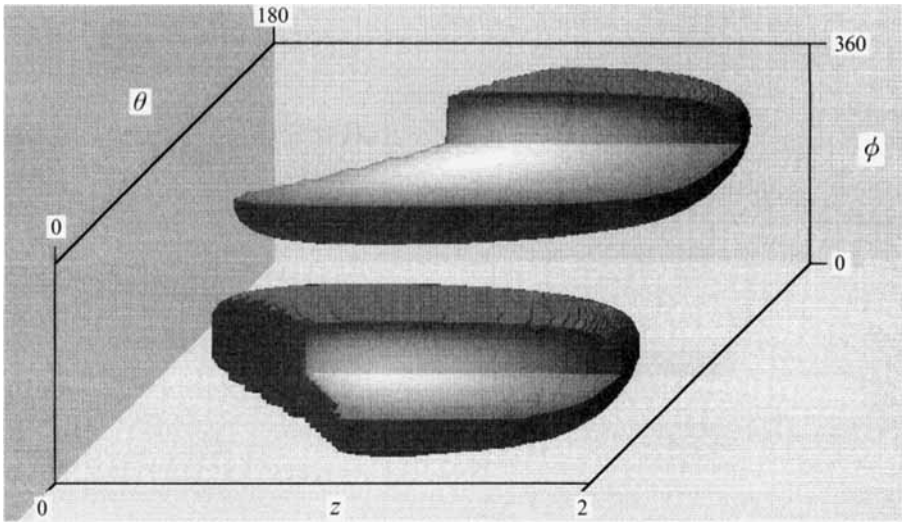

FIGURE 18. As figure 17 but for a gap width of $\lambda = 4.0$.

the same profiles derived from the self-consistent calculations for a concentration of $c = 0.1$ and a gap width of $\lambda = 6$ is shown in figure 22. At low concentrations, the asymptotic theory reproduces the qualitative shape of the extra stress and velocity profile. At higher concentrations, $c > 0.25$, the asymptotic theory differs significantly from the self-consistent theory.

In the small gap limit where $\lambda \to 0$ the above asymptotic theory applies and can be simplified. Taking the limit $\lambda \to 0$, the only result that changes is the shape function $S(z)$ which becomes

$$S(z) = \tfrac{2}{3}z^3. \tag{7.6}$$

and is identical to the small gap shape function derived earlier for shear flow.

As was done for the analysis of shear flow in the previous section the asymptotic theory for both small concentration and small gap width can be used to derive predictions of a suspension's effective properties. In the next subsection we will compare the effective rheology predicted via the fully self-consistent theory with this simple asymptotic theory.

7.2. *Effective rheology*

For pressure-driven flow, the effective viscosity is defined as the ratio of the volumetric flow rate of the Newtonian solvent to the volumetric flow rate of the suspension at the same pressure drop. Since the velocity profile for the Newtonian case is known, the average effective viscosity can be written concisely as

$$\frac{\mu_{eff}}{\mu} = \frac{\lambda^2}{6}\left(\int_0^{\lambda} \bar{u}(z)\mathrm{d}z\right)^{-1}. \tag{7.7}$$

Employing the velocity profile predicted from the asymptotic theory in the preceding section, an analytic expression for the dependence of the effective viscosity on total gap width can be derived. Using equation (7.5) to calculate the approximation to the volumetric flow rate for a confined fibre suspension and substituting into

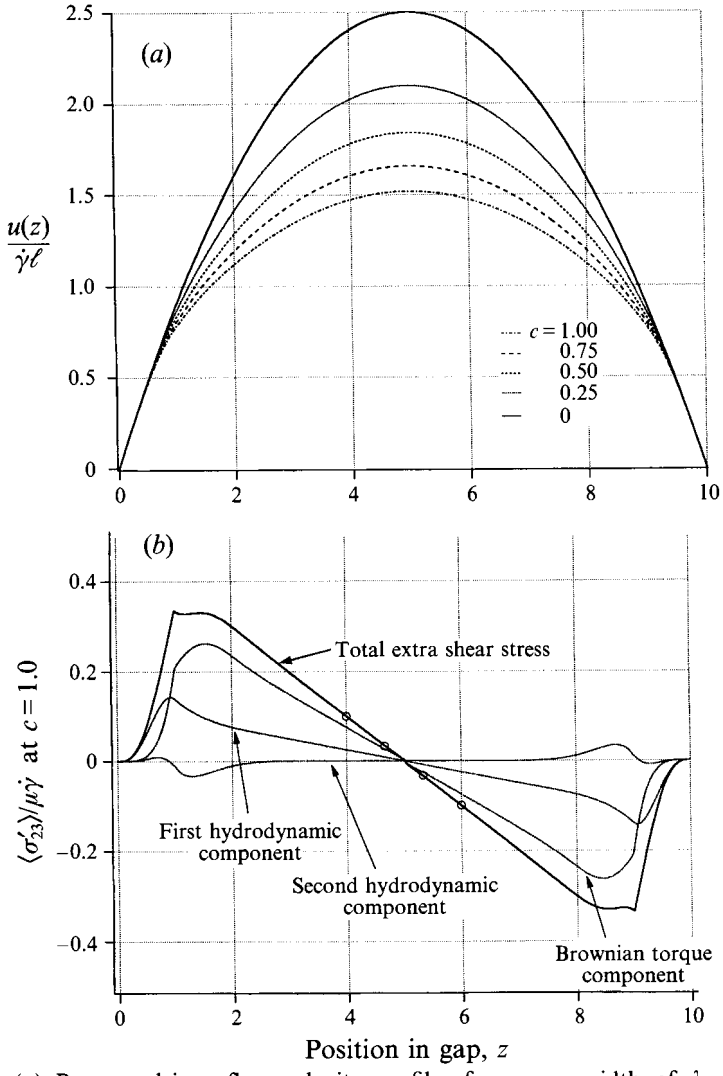

FIGURE 19. (*a*) Pressure-driven flow velocity profiles for a gap width of $\lambda = 10.0$ and fibre concentrations of $0 \leqslant c \leqslant 1.0$. (*b*) Extra shear stress profiles for $\lambda = 10.0$ and $c = 1.0$. Open circles denote the extra shear stress predicted by the unbound suspension theory of Hinch & Leal (1972) evaluated at a fibre concentration of $c = 1.0$ and at the local shear rate.

equation (7.7) one can derive

$$\frac{\mu_{eff}}{\mu} = 1 + \tfrac{4}{3}\pi^2 M(\lambda)c$$

$$\times \begin{cases} \dfrac{\lambda^3\,(7168 - 195\lambda^2)}{1720320} & \text{for } 0 \leqslant \lambda \leqslant 2 \\ \dfrac{(6\lambda^8 - 27\lambda^7 - 651\lambda^6 + 5964\lambda^5 - 8190\lambda^4 + 25648\lambda^3 - 185136\lambda^2 + 422208\lambda - 299728)}{107520\lambda^3} & \text{for } 2 \leqslant \lambda \leqslant 4 \\ \dfrac{7168\lambda^3 - 38640\lambda^2 + 72684\lambda - 46045}{6720\lambda^3} & \text{for } \lambda \geqslant 4. \end{cases} \tag{7.8}$$

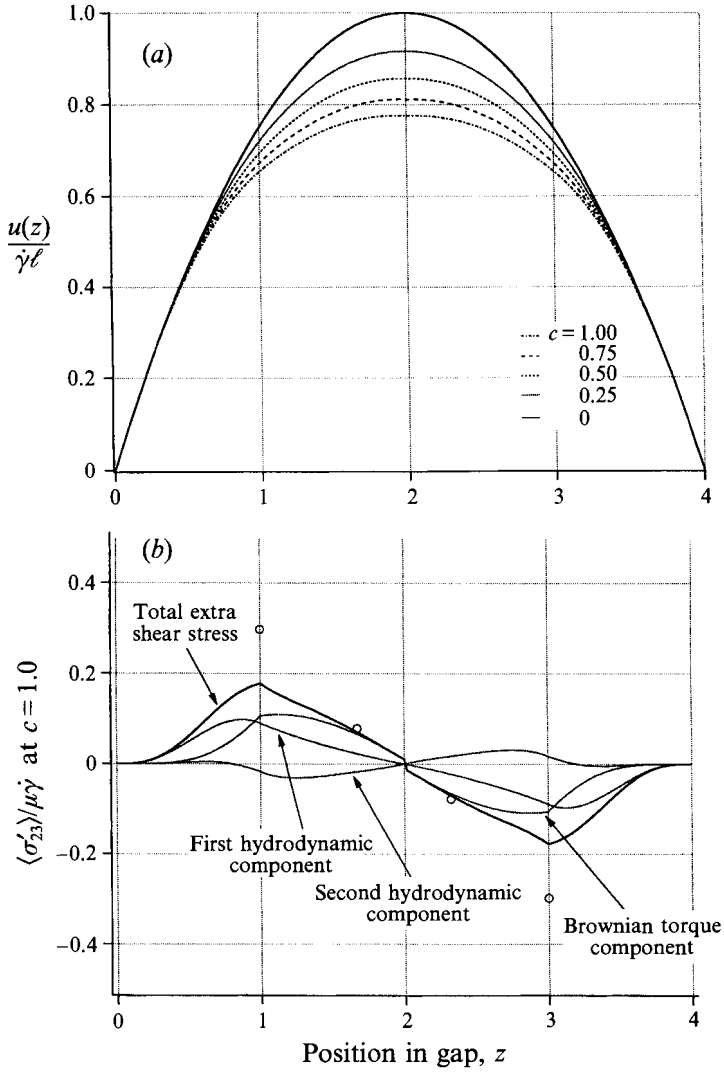

FIGURE 20. As figure 19 but for a gap width of $\lambda = 4.0$.

The limiting behaviour for the effective viscosity in a small gap is,

$$\lim_{\lambda \to 0} \frac{\mu_{eff}}{\mu} = 1 + \tfrac{4}{3}\pi^2 M(\lambda)\, c\, \tfrac{\lambda^3}{240}, \tag{7.9}$$

whose divisor is an order of magnitude larger, 240 compared to 48, than the divisor of the effective viscosity taken in the same limit for shear flow in the previous section, cf. equation (6.14).

In the large gap limit where $\lambda \gg 1$, the effective viscosity under shear flow scales as

$$\lim_{\lambda \gg 1} \frac{\mu_{eff}}{\mu}\bigg|_{\text{shear flow}} = 1 + \tfrac{4}{3}\pi^2 M(\lambda)\, c\, \left(\tfrac{64\lambda - 115}{60\lambda}\right). \tag{7.10}$$

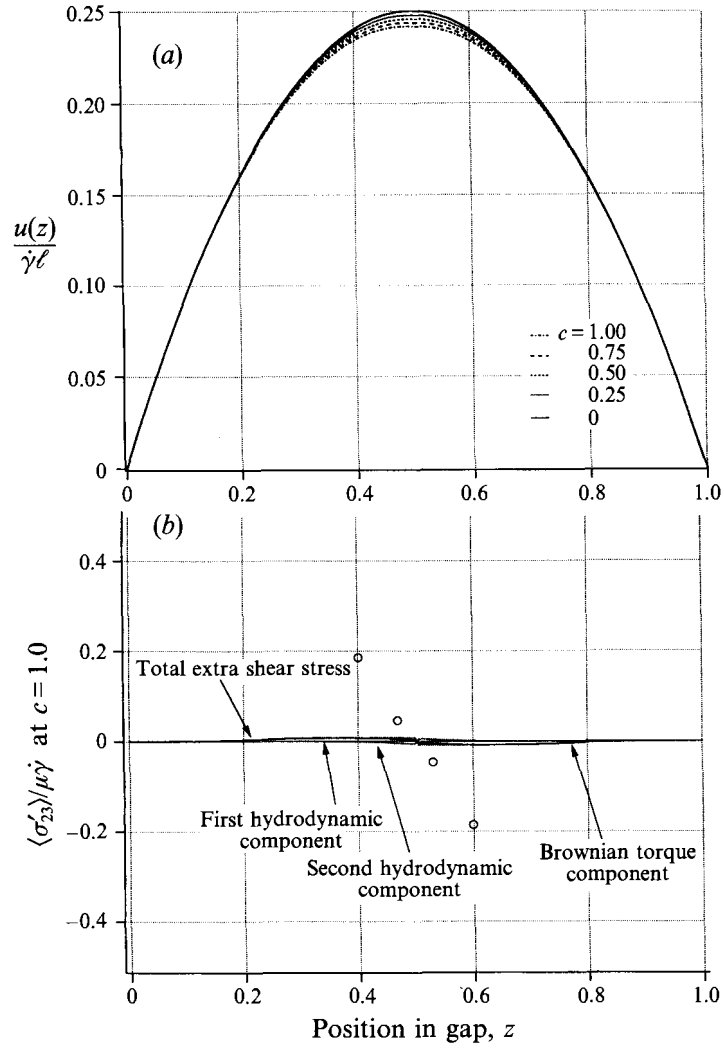

FIGURE 21. As figure 19 but for a gap width of $\lambda = 1.0$.

Under pressure-driven flow, the limiting behaviour of the effective viscosity is,

$$\lim_{\lambda \gg 1} \frac{\mu_{eff}}{\mu}\bigg|_{\text{pressure-driven flow}} = 1 + \tfrac{4}{3}\pi^2 M(\lambda)\, c\, \left(\tfrac{64\lambda - 345}{60\lambda}\right). \tag{7.11}$$

Comparison of equations (7.10) and (7.11) indicates that for pressure-driven flow, *significantly larger gaps are required to achieve the same increase in effective viscosity*, because of the coefficient $-\frac{115}{60} = -\frac{23}{12}$ in shear versus $-\frac{345}{60} = -\frac{69}{12}$ in Poiseuille flow.

Plotted in figure 23 is the effective viscosity as defined by equation (7.7) for various gap widths and concentrations of fibres. As before, the data are plotted in three ways. First, figure 23(*a*) presents the effective viscosity data normalized for a reduced available volume while figure 23(*b*) presents the effective viscosity for a confined suspension in equilibrium with an unbound suspension of number density n. Finally, figure 23(*c*) presents the effective viscosity once the dependence on gap width has been factored out according to the effective viscosity predictions of the asymptotic theory,

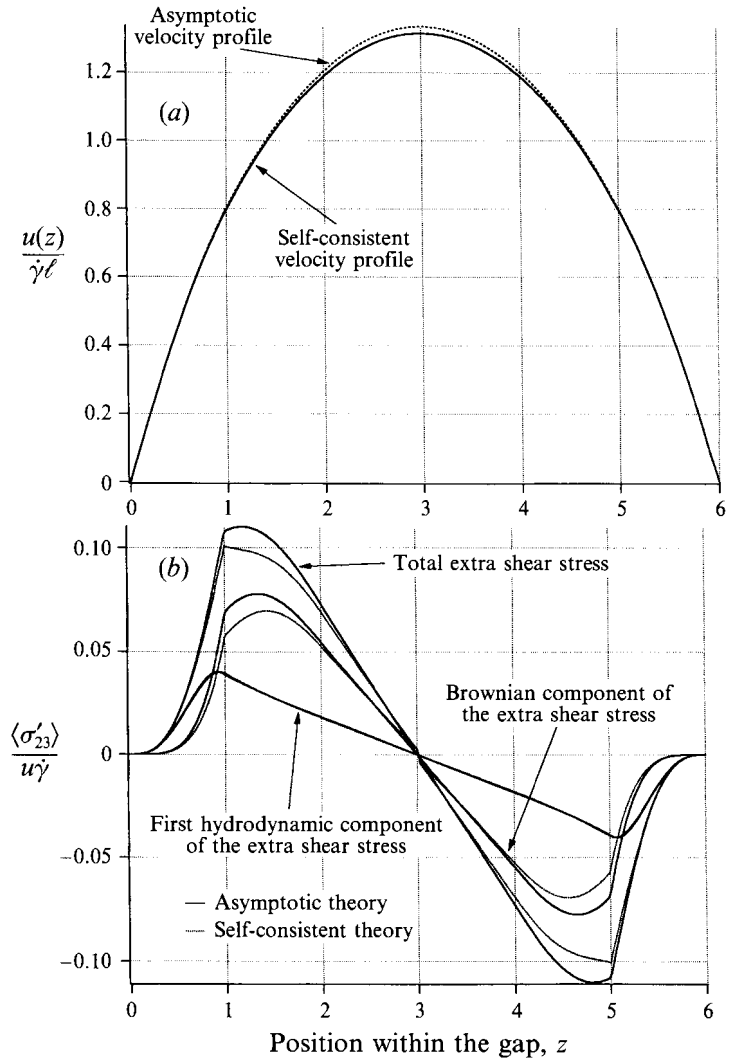

FIGURE 22. (*a*) Pressure-driven flow velocity and (*b*) extra shear stress profiles for a gap width of $\lambda = 6$ and a fibre concentration of $c = 0.10$ as predicted by the the self-consistent, nonlocal theory and the dilute asymptotic theory.

equation (7.8). Comparing these plots with the same plots for shear flow in figure 12 shows that the pressure-driven effective viscosities take considerably larger gaps to reach the anticipated unbound effective viscosities. In figure 23(*c*), the nearly constant values of the effective viscosity data derived from the self-consistent calculations when rescaled with the asymptotic theory suggest that the main assumption of the asymptotic theory is correct, namely that the primary effect of the boundary is to reduce the allowed set of orientation angles for fibres near the walls.

The effective viscosity defined by equation (7.7) determines the viscosity that a Newtonian solution would have in order to produce the same volumetric flow rate as the fibre suspension at the same axial pressure drop. Given a Newtonian solution with the effective viscosity predicted by equation (7.7), and the same maximum velocity as the fibre suspension at the centre of the channel, the slip velocity is defined as the

velocity that the Newtonian solution would have at the walls of the channel. Defined as such, the slip velocity is a measure of the degree to which a fibre suspension confined in a channel alters the natural, parabolic velocity profile of a Newtonian fluid. The larger the slip velocity, the more the presence of the fibres distorts the parabolic profile. Plotted in figure 24 are slip velocities made dimensionless with the centreline velocity in figure 24(*a*) and with the characteristic velocity $\dot{\gamma}\ell$ in figure 24(*b*). As was the case with shear flow, the slip relative to the maximum velocity reaches a maximum value around $\lambda = 5$ and then declines. On the other hand, the slip velocity relative to the velocity $\dot{\gamma}\ell$ rapidly climbs to a maximum value as the gap width increases. Comparison of the slip velocity under shear flow made dimensionless with the same characteristic velocity, $\dot{\gamma}\ell$, to the slip velocity under pressure-driven flow shows that the magnitude of the slip is much smaller for pressure-driven flow; cf. figures 13(*b*) and 24(*b*). Additionally, the slip expected for infinitely large gaps made dimensionless with $\dot{\gamma}\ell$ as a function of concentration is plotted in figure 14. Direct comparison can be made with the slip velocities calculated for shear flow in this figure since they have been non-dimensionalized by the same quantity. As shown by figure 14, the slip velocity under pressure-driven flow is a nonlinear function of fibre concentration. At low concentrations both shear and pressure-driven flow slip velocities are comparable. However, at larger concentrations, the slip velocity for pressure-driven flow is much smaller than the predicted slip for shear flow.

8. Comparison with experiments

Unfortunately the experimental difficulties associated with measuring velocity profiles for suspensions confined to regions whose size is of the order of a micron has prevented measurement of velocity profiles to which we can compare our theory. However, direct comparisons can be made with our theoretical predictions for the effective viscosity and experimentally measured effective viscosities of fibre suspensions in flow through porous media.

Sorbie & Huang (1991) measured the pressure drop associated with passing a dilute suspension of Xanthan gum through a packed bed of spheres. Since they only used a bed packed with one fixed size of spheres, from which they derived a hydrodynamic pore size, their effective viscosity measurements can only be compared to one gap width in our work. For a pore size of 14.0 μm and a fibre half-length of 0.5 μm the dimensionless gap width for their experiments is $\lambda = 28.0$. Lacking accurate size data for Xanthan gum, the concentration parameters for our theory were determined as follows. Based on the work of Hinch & Leal (1972), the zero shear viscosity for an unbound suspension of slender rigid fibres should be

$$\frac{\mu_{eff}}{\mu} = 1 + c\frac{16\pi}{45}. \tag{8.1}$$

Using the unbound suspension effective viscosities reported by Sorbie & Huang (1991), the concentration was calculated for each solution that passed through the packed bed. Calculated this way, the concentration parameter ranged from $c = 0.25$ to $c = 2.60$ in the experiments of Sorbie & Huang (1991).

Plotted in figure 25 is the effective viscosity made dimensionless with the solute viscosity predicted from the fully self-consistent nonlocal theory presented in this paper along with the experimentally measured effective viscosities of Sorbie & Huang (1991). While our theory is strictly valid only for small concentrations where $c \ll 1$, our the-

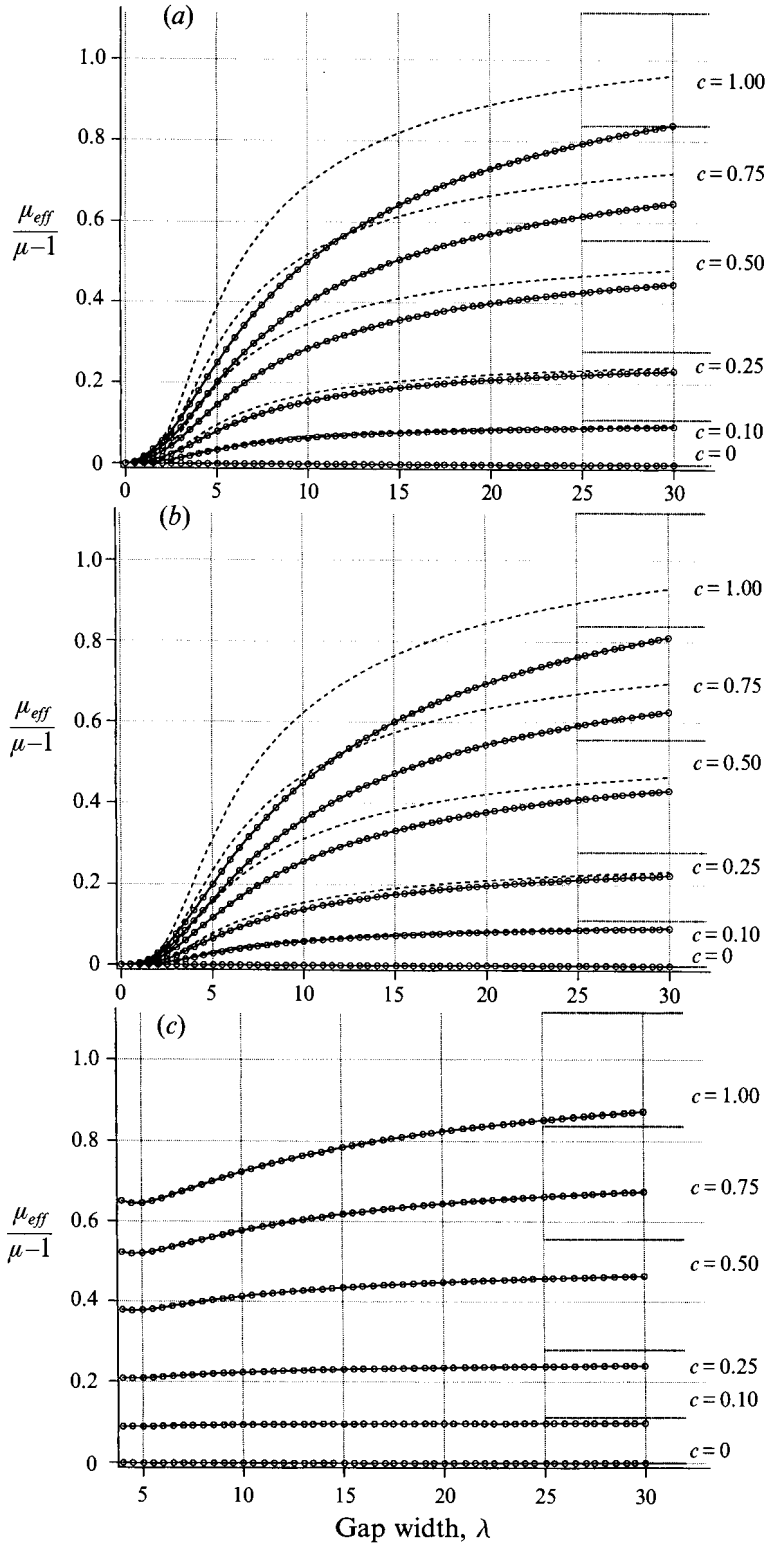

FIGURE 23. For caption see facing page

ory compares very well with the experiments up to $c \approx 2.0$. For fibre concentrations greater than 2.0 our predictions fall below their experimental measurements. This can be attributed to multi-particle effects which are important at higher concentrations but ignored in our theory.

Additional experiments were performed by Chauveteau (1982) where he passed dilute and concentrated Xanthan solutions through fine capillaries while measuring effective viscosities. While Chauveteau performed experiments with many different Xanthan solutions at different concentrations, the only data available in print are for a concentrated suspension of Xanthan where $c = 2.69$ determined in the same way as mentioned above. However, Chauveteau employed several different capillary sizes in his experiments thus spanning dimensionless gap widths from $\lambda = 30$ to $\lambda = 2$. Plotted in figure 26 are the effective viscosities measured by Chauveteau (1982) and the effective viscosities predicted by our fully self-consistent, nonlocal theory. There is a constant underestimation of the effective viscosity by our theory at these high fibre concentrations, but that is to be expected based on the comparison with the results of Sorbie & Huang (1991). However, the theory does an excellent job in predicting the decay of the effective viscosity as the gap with is reduced.

9. Conclusions

Within this work we have developed a nonlocal theory for the stress in bound suspensions of rigid fibres. Calculation of the nonlocal stress requires the fibres' probability density function and the velocity field. Through a Fokker–Plank description of the probability and a momentum balance, a complete coupled set of integral-differential equations was derived to describe the model system of a suspension of slender fibres confined between two infinite, parallel plates. Under both shear and pressure-driven flow, the nonlocal extra stress was dominated, at low Péclet number, by contributions from Brownian torques. Near the fluid boundaries, the Brownian component of the extra stress decayed to zero at a distance of one full particle length. The weaker hydrodynamic component of the extra stress decayed to zero at the wall, but over a distance comparable to a fibre half-length. Also, for both shear and pressure-driven flows, the hydrodynamic component of the extra stress was the dominant contribution to the extra stress for very small gap widths.

In addition to shear stresses, normal stress differences were calculated. For all gap widths the first normal stress difference remained positive over the entire gap while increasing to a maximum before approaching zero at the fluid boundaries. The increase in the first normal stress difference before it decreased to zero at the boundary is a concentration effect disappearing as the concentration diminishes. The second normal stress difference was smaller in magnitude than the first normal stress difference for large gap widths. However near a boundary, and across the entire gap for small gap widths, the second normal stress difference becomes positive regardless of

FIGURE 23. Effective viscosity of a confined suspension under pressure-driven flow as a function of gap width and fibre concentration. In all three figures the open circles connected with lines represent the self-consistent, nonlocal theory, while the large-dashed lines represent the asymptotic theory and the small-dashed lines represent the predictions of Hinch & Leal (1972) for the effective viscosity of an unbound fibre suspension at the indicated concentration. In (*a*) the data are normalized for a reduced available volume, while in (*b*) and (*c*) the data are normalized to be in equilibrium with an unbound suspension at the same concentration as described in the text.

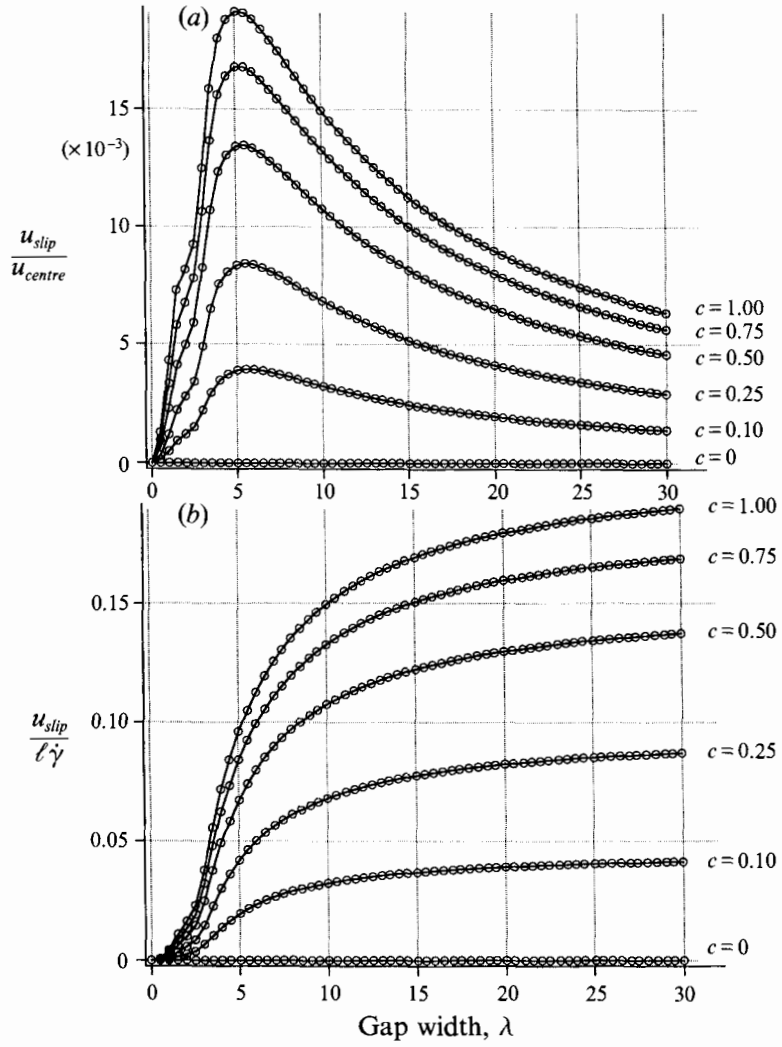

FIGURE 24. Slip velocity for a confined fibre suspension under pressure-driven flow as a function of gap width and concentration. In (*a*) the slip velocity is made dimensionless with the velocity at the centre of the channel, u_{centre}, while in (*b*) the slip velocity is made dimensionless with the characteristic velocity $\dot{\gamma}\ell$. Open circles connected with lines represent predictions by the self-consistent, nonlocal theory.

the fibre concentration. The positive second normal stress difference can be attributed to the restricted rotational movements of fibres near the flow boundaries. We speculate that perhaps rapid changes in the first and second normal stress differences near the fluid boundaries may cause bulk flow instabilities found in polymer jets exiting orifices in low Reynolds number flows (Piau, El Kissi & Tremblay 1990).

To better understand the predictions of the self-consistent theory, simple asymptotic theories were developed in the limit of small fibre concentration and in the limit of small gap width for both shear and pressure-driven flows. A primary assumption of these theories was that the probability density function for fibres confined between two infinite and parallel plates was the same as the probability density function for fibres in an unbound fluid suspension except that fibre configurations which penetrated

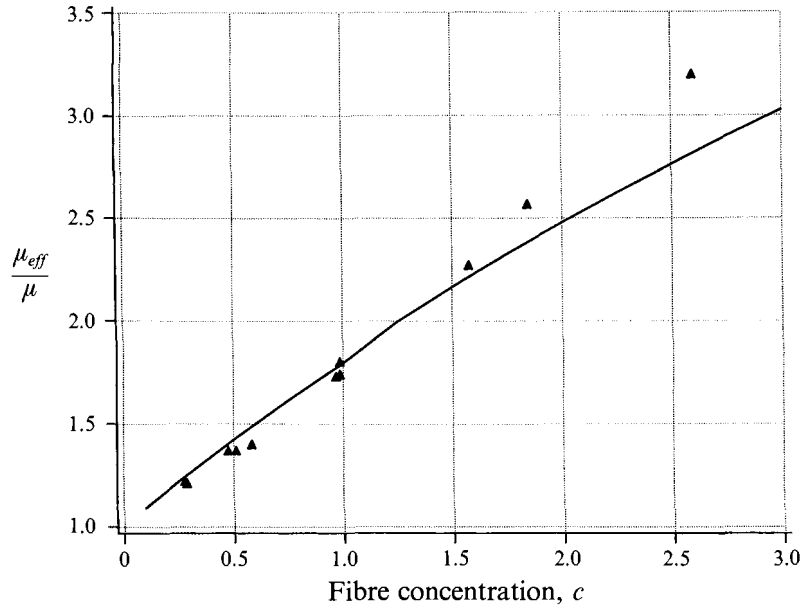

FIGURE 25. Comparison of the effective viscosities measured by Sorbie & Huang (1991) at a fixed gap width of $\lambda = 28.0$ and fibre concentrations $0.30 \leqslant c \leqslant 2.55$ to the effective viscosity predicted by the self-consistent, nonlocal theory the same gap width. Dark triangles denote the measurements of Sorbie & Huang while the solid line represents the predictions of the self-consistent, nonlocal theory.

the fluid boundaries, were not allowed. Thus the asymptotic theories neglected the zero particle flux conditions at the fluid boundaries replacing the no-flux condition with truncation of the probability density function for unallowed fibre configurations. Qualitatively, the asymptotic theories worked well in predicting the general shape of the extra stress and velocity profiles at low fibre concentrations. However at higher concentrations, the asymptotic theories performed poorly. Rederiving the asymptotic theories to make them self-consistent in extra stress and velocity while making the same assumptions regarding the probability density function may provide a simple, analytic theory that does well at moderate fibre concentrations.

The effective rheology was investigated and predicted by the self-consistent, nonlocal theory, and the asymptotic theories. When the confined suspension's properties were quantified in terms of an effective viscosity, both the shear and pressure-driven flow effective viscosities decreased with gap width. The scaling of the effective viscosities derived from the asymptotic theories did an excellent job at low concentrations in mimicking the self-consistent, nonlocal theory. When compared to experimental measurements, the effective viscosity of the self-consistent, nonlocal theory quantitatively predicted experimentally measured values at moderate and low fibre concentrations at a small gap width as reported by Sorbie & Huang (1991). At high fibre concentrations, the self-consistent, nonlocal theory under-predicted the effective viscosity, giving qualitative but not quantitative agreement with the experimental measurements.

A final effective property predicted by the self-consistent, nonlocal theory was the slip velocity of the suspension near the confining boundaries. Under both shear and pressure-driven flows, the slip velocity made dimensionless with the characteristic velocity $\dot{\gamma}\ell$ grew with increasing gap width and reached a plateau as $\lambda \to \infty$. As a function of fibre concentration, the slip velocity at infinite gap width was a linear

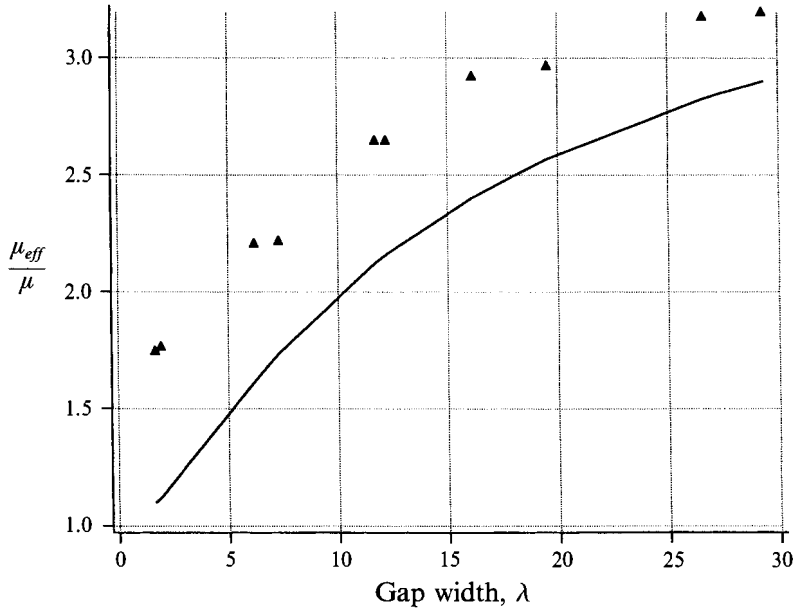

FIGURE 26. Comparison of the effective viscosities measured by Chauveteau (1982) for gap widths $2.0 \leqslant \lambda \leqslant 29.0$ and a fibre concentration of $c \approx 2.69$ to predictions by the self-consistent, nonlocal theory at the same concentration. Dark triangles denote the measurements of Chauveteau while the solid line represents the predictions of the self-consistent, nonlocal theory.

function of concentration for shear flow. For pressure-driven flow, the slip velocity is comparable to the slip under shear flow at very low concentrations and infinite gap widths. However, as the fibre concentration increases, growth of the slip velocity in pressure-driven flow is slower, resulting in a nonlinear dependence of the slip velocity on fibre concentration.

E.S.G.S. would like to thank the National Science Foundaton for funding this work through a Presidential Young Investigator Award, grant number CTS-9057284, and the David and Lucile Packard foundation for funding through their fellowship program.

REFERENCES

AUBERT, J. H. & TIRRELL, M. 1982 Effective viscosity of dilute polymer solutions near confining boundaries. *J. Chem. Phys.* **77**, 553–561.

BATCHELOR, G. K. 1970 Slender-body theory for particles of arbitrary cross-section in Stokes flow. *J. Fluid Mech.* **44**, 419–440.

BATCHELOR, G. K. 1971 The stress generated in a non-dilute suspension of elongated particles by pure straining motion. *J. Fluid Mech.* **46**, 813–829.

BERRY, D. H. & RUSSEL, W. B. 1987 The rheology of dilute suspensions of slender rods in weak flows. *J. Fluid Mech.* **180**, 475–494.

BIRD, R. B. & WARNER, H. R. 1971 Hydrodynamic interaction effects in rigid dumbbell suspensions. I. Kinetic theory. *Trans. Soc. Rheol.* **15**, 741–750.

BRADY, J. F. 1993 Brownian motion, hydrodynamics, and the osmotic pressure. *J. Chem. Phys.* **98**, 3335–3341.

BRENNER, H. 1974 Rheology of a dilute suspension of axisymmetric brownian particles. *Intl. J. Multiphase Flow* **1**, 195–341.

BRUNN, P. O. 1976 The effect of a solid wall for the flow of dilute macromolecular solutions. *Rheol. Acta* **15**, 23–29.

BRUNN, P. O. & GRISAFI, S. 1987 Wall effects in simple shear of dilute polymer solution: exact results for very narrow and very wide channels. *J. Non-Newtonian Fluid Mech.* **24**, 343–363.

CHANDRASEKHAR, S. 1943 Stochastic problems in physics and astronomy. *Rev. Mod. Phys.* **15**, 1–89.

CHAUVETEAU, G. 1982 Rodlike polymer solution flow through fine pores: influence of pore size on rheological behaviour. *J. Rheol.* **26**, 111–142.

COHEN, Y. & METZNER, A. B. 1985 Apparent slip flow of polymer solutions. *J. Rheol.* **29**, 67–102.

DOI, M. & EDWARDS, S. F. 1989 *The Theory of Polymer Dynamics.* Oxford Science Publications.

GIESEKUS, V. H. 1962 Elasto-viskose flüssigkeiten, für die in stationären schichtströmungen sämtliche normalspannungskomponenten verschieden groß sind. *Rheol. Acta* **2**, 50–62.

HINCH, E. J. 1977 An averaged-equation approach to particle interactions in a fluid suspension. *J. Fluid Mech.* **83**, 695–720.

HINCH, E. J. & LEAL, L. G. 1972 The effect of Brownian motion on the rheological properties of a suspension of non-spherical particles. *J. Fluid Mech.* **52**, 683–712.

HINCH, E. J. & LEAL, L. G. 1975 Constitutive equations in suspension mechanics. Part 1. General formulation. *J. Fluid Mech.* **M1**, 481–495.

HINCH, E. J. & LEAL, L. G. 1976 Constitutive equations in suspension mechanics. Part 2. Approximate forms for a suspension of rigid particles affected by Brownian rotations. *J. Fluid Mech.* **76**, 187–208.

KIRKWOOD, J. G. & RISEMAN, J. 1948 The intrinsic viscosities and diffusions constants of flexible macromolecules in solution. *J. Chem. Phys.* **16**, 565–573.

LARSON, R. G. 1988 *Constitutive Equations for Polymer Melts and Solutions*. Butterworths.

LEAL, L. G. & HINCH, E. J. 1971 The effect of weak Brownian rotations on particles in shear flow. *J. Fluid Mech.* **46**, 685–703.

MAGDA, J. J., TIRRELL, M. & DAVIS, H. 1988 The transport properties of rod-like particles. II. Narrow slit pores. *J. Chem. Phys.* **88**, 1207–1213.

MARION, J. B. & THORNTON, S. T. 1988 *Classical Dynamics of Particles and Systems*, 3rd Edn. Harcourt Brace Jovanovich Inc.

MAVRANTZAS, V. G. & BERIS, A. N. 1992 Theoretical study of wall effects on the rheology of dilute polymer solutions. *J. Rheol.* **36**, 175–213.

MCQUARRIE, D. A. 1976 *Statistical Mechanics.* Harper Collins.

MÜLLER-MOHNSSEN, H., WEISS, D. & TIPPE, A. 1990 Concentration dependent changes of apparent slip in polymer solution flow. *J. Rheol.* **34**, 223–244.

NITSCHE, J. M. 1991 Hydrodynamic coupling and non-equilibrium distribution in pore diffusion of nonspherical fine particles. *Particulate Sci. Tech.* **9**, 135–148.

NITSCHE, J. M. & BRENNER, H. 1990 On the formulation of boundary conditions for rigid non-spherical brownian particles near solid walls: applications to orientation-specific reactions with immobilized enzymes. *J. Colloid Interface Sci.* **138**, 21–41.

PIAU, J. M., EL KISSI, N. & TREMBLAY, B. 1990 Influence of upstream instabilities and wall slip on melt fracture and sharkskin phenomena during silicones extrusion through orifice dies. *J. Non-Newtonian Fluid Mech.* **34**, 145–180.

RALLISON, J. M. 1988 Brownian diffusion in concentrated suspensions of interacting particles. *J. Fluid Mech.* **186**, 471–500.

RISEMAN, J. & KIRKWOOD, J. G. 1950 The intrinsic viscosity, translational and rotatory diffusion constants of rod-like macromolecules in solution. *J. Chem. Phys.* **18**, 512–516.

RUBÍ, J. M., PÉREZ-MADRID, A. & SALUEÑA, C. 1990 On transport coefficients and relaxation phenomena in ferrofluids: I. Viscoelastic behaviour and relaxation. *Physica* A **163**, 791–803.

RUSSEL, W. B., HINCH, E. J., LEAL, L. G. & TIEFFENBRUCK, G. 1977 Rods falling near a vertical wall. *J. Fluid Mech.* **83**, 273–287.

SALUEÑA, C. PÉREZ-MADRID, A. & RUBÍ, J. M. 1990 On transport coefficients and relaxation phenomena in ferrofluids: II. Effect of an external flow. *Physica* A **169**, 375–392.

SHAQFEH, E. S. G. 1988 A nonlocal theory for the heat transport in composites containing highly conducting fibrous inclusions. *Phys. Fluids* **31**, 2405–2425.

SHAQFEH, E. S. G. & FREDRICKSON, G. H. 1990 The hydrodynamic stress in a suspensions of rods. *Phys. Fluids* A **2**, 7–24.

SORBIE, K. S. & HUANG, Y. 1991 Rheological and transport effects in the flow of low-concentration xanthan solution through porous media. *J. Colloidal Interface Sci.* **145**, 74–89.

STEWART, W. E. & SORENSEN, J. P. 1972 Hydrodynamic interaction effects in rigid dumbbell suspensions. II. Computations for steady shear flow. *Trans. Soc. Rheol.* **16**, 1–13.

VARGAS, L. DE, PÉREZ-GONZÁLEZ, J. & ROMERO-BARENQUE, J. 1993 Experimental evidence of slip development in capillaries and a method to correct for end effects in the flow of xanthan solutions, *J. Rheol.* **37**, 867–878.